Penn Libraries
UNIVERSITY of PENNSYLVANIA

University of Pennsylvania
ScholarlyCommons

Publicly Accessible Penn Dissertations

Summer 8-13-2010

Jamming Phase Diagram, Effective Temperature, and Heterogeneous Dynamics of Model Glass-Forming Liquids

Thomas K. Haxton
University of Pennsylvania, haxton@sas.upenn.edu

Follow this and additional works at: http://repository.upenn.edu/edissertations

Part of the Condensed Matter Physics Commons

Jamming Phase Diagram, Effective Temperature, and Heterogeneous Dynamics of Model Glass-Forming Liquids

Abstract

We establish that the behavior of fluids consisting of repulsive spheres under the combined effects of pressure p, temperature T, and applied shear stress s can be organized in a jamming phase diagram parameterized by the dimensionless quantities T/pd^3, s/p, and pd^3/e, where d is the diameter of the spheres and e is the interaction energy scale. The jamming phase diagram describes the three-dimensional parameter space as the product of an equilibrium plane at $s/p=0$ and a hard sphere plane at $pd^3/e=0$. Near the hard sphere plane, the jamming phase diagram is universal in the sense that material properties are insensitive to the details of the interaction potential. We demonstrate that within the universal regime, the conventional approach to the dynamic glass transition along a decreasing temperature trajectory is equivalent to the colloidal glass transition approach along an increasing pressure trajectory. Defining the dynamic glass transition by where a dimensionless relaxation time equals a large but arbitrary value, we measure a two-dimensional dynamic glass transition surface whose precise location depends on the choice of time scale but which always encloses the singular point at the origin, $T/pd^3=s/p=pd^3/e=0$. We show that at finite shear stress, the effective temperature T_{eff} fluidizes the system in a similar way as the environment temperature T fluidizes the system in the absence of shear. We demonstrate that the dynamic glass transition surface is largely controlled a single parameter, the dimensionless effective temperature T_{eff}/pd^3, that describes the competition between low frequency fluctuations and the confining pressure. Even well into the fluid portion of the jamming phase diagram, we show that relaxation is largely controlled by this single parameter, regardless of whether the fluctuations are created by temperature or shear. Finally, by investigating correlations in the dynamics as a function of length scale a and time scale t, we identify two types of pairs (a, t) over which the dynamics are maximally correlated, suggesting that kinetic heterogeneity is a general feature of dynamical crossovers and not necessarily an indication of an impending thermodynamic transition.

Degree Type
Dissertation

Degree Name
Doctor of Philosophy (PhD)

Graduate Group
Physics & Astronomy

First Advisor
Andrea J. Liu

Keywords
glass transition, jamming, effective temperature, dynamic heterogeneity, hard spheres

Subject Categories
Condensed Matter Physics

JAMMING PHASE DIAGRAM, EFFECTIVE TEMPERATURE, AND

HETEROGENEOUS DYNAMICS OF MODEL GLASS-FORMING LIQUIDS

Thomas K. Haxton

A DISSERTATION

in

Physics and Astronomy

Presented to the Faculties of the University of Pennsylvania

in

Partial Fulfillment of the Requirements for the

Degree of Doctor of Philosophy

Supervisor of Dissertation

Signature _____

Andrea J. Liu

Professor of Physics and Astronomy

Graduate Group Chairperson

Signature _____

Ravi K. Sheth, Professor of Physics and Astronomy

Dissertation Committee

Vijay Balasubramanian, Professor of Physics and Astronomy

Douglas J. Durian, Professor of Physics and Astronomy

Randall D. Kamien, Professor of Physics and Astronomy

Arjun G. Yodh, Professor of Physics and Astronomy

Jamming phase diagram, effective temperature, and heterogeneous dynamics of model glass-forming liquids

COPYRIGHT

2010

Thomas Kirk Haxton

ABSTRACT

JAMMING PHASE DIAGRAM, EFFECTIVE TEMPERATURE, AND
HETEROGENEOUS DYNAMICS OF MODEL GLASS-FORMING LIQUIDS

Thomas K. Haxton

Andrea J. Liu

We establish that the behavior of fluids consisting of repulsive spheres under the combined effects of pressure p, temperature T, and applied shear stress σ can be organized in a jamming phase diagram parameterized by the dimensionless quantities T/pd^3, σ/p, and pd^3/ϵ, where d is the diameter of the spheres and ϵ is the interaction energy scale. The jamming phase diagram describes the three-dimensional parameter space as the product of an equilibrium plane at $\sigma/p = 0$ and a hard sphere plane at $pd^3/\epsilon = 0$. Near the hard sphere plane, the jamming phase diagram is universal in the sense that material properties are insensitive to the details of the interaction potential. We demonstrate that within the universal regime, the conventional approach to the dynamic glass transition along a decreasing temperature trajectory is equivalent to the colloidal glass transition approach along an increasing pressure trajectory. Defining the dynamic glass transition by where a dimensionless relaxation time equals a large but arbitrary value, we measure a two-dimensional dynamic glass transition surface whose precise location depends on the choice of time scale but which always encloses the singular point at the origin, $T/pd^3 = \sigma/p = pd^3/\epsilon = 0$. We show that at finite shear stress, the effective temperature T_{eff} fluidizes the system in a similar way as the environment temperature T fluidizes the system in the absence of shear. We

iii

demonstrate that the dynamic glass transition surface is largely controlled a single parameter, the dimensionless effective temperature T_{eff}/pd^3, that describes the competition between low frequency fluctuations and the confining pressure. Even well into the fluid portion of the jamming phase diagram, we show that relaxation is largely controlled by this single parameter, regardless of whether the fluctuations are created by temperature or shear. Finally, by investigating correlations in the dynamics as a function of length scale a and time scale t, we identify two types of pairs (a, t) over which the dynamics are maximally correlated, suggesting that kinetic heterogeneity is a general feature of dynamical crossovers and not necessarily an indication of an impending thermodynamic transition.

Contents

List of Figures

Chapter 1

Introduction

1.1 Glass transition

Although people have been making glass for millenia, we still lack a clear physical understanding of how glass forms. Generally defined as any transition from a fluid to a disordered solid state, the glass transition is a ubiquitous phenomenon that remains one of the oldest and most difficult problems in condensed matter physics [31].

One way to form glass is to quench a liquid from a high-temperature and typically equilibrium fluid state to a disordered solid state at lower temperature. As the temperature lowers, the equilibrium state predicted by statistical mechanics changes, but the constituent particles making up the liquid also become less mobile, so it takes longer for the liquid to relax to an equilibrium configuration. If the quench is fast enough, the dynamics slow down so dramatically that the liquid becomes stuck out of equilibrium. Amazingly, the structural relaxation time of

1

a good glass-forming liquid increases by a factor of 10^{14} when the temperature drops only by a factor of 2. If the system has an equilibrium liquid-to-crystal phase transition, the dynamic slowing down is often sufficient to suppress crystallization. Below the melting temperature, the liquid is said to be supercooled. At sufficiently low temperature, the structural relaxation time and shear viscosity become large compared with the time and stress scales of typical mechanical tests; that is, the system becomes a solid. The glass transition from a fluid to an amorphous solid is not a true phase transition because it occurs out of equilibrium; rather, it is a dynamical transition that depends on how long one is willing to wait in order to see if the glass-former will flow.

The glass transition is a widespread phenomenon in nature and human industry. Glass formed from a variety of liquids exhibit common phenomena in both the supercooled and solid regimes. As supercooled liquids, they exhibit a faster-than-exponential dependence of relaxation time on inverse temperature and a broad relaxation spectrum characterized by stretched-exponential correlation functions. As solids, they exhibit similar low-energy excitations characterized by a "boson peak" of excess low-frequency vibrational modes [95] and an anomalous temperature-dependence of the specific heat at low temperatures. Such similarities suggest that universal physical mechanisms may control their behavior.

1.2   Jamming Phase Diagram

Not only do a wide variety of homogeneous liquids form glasses, but so do many complex fluids such as colloids, foams, and emulsions, mixtures of one phase of

matter in another [21]. Complex fluids have many useful applications because their mechanical properties are sensitive to external stress. Tightly packed complex fluids–dense colloidal suspensions and emulsions, dry foams, and granular materials–behave like solids under small stresses but can be made to flow under larger stresses. Both the linear and nonlinear mechanical response of a large class of such "soft glassy materials" show many similarities: the linear response to shear stress is viscoelastic, while the nonlinear response exhibits shear thinning, a steady-state shear viscosity that decreases with increasing shear strain rate [96].

When the elements of the dispersed phase of a complex fluid are small enough, they undergo Brownian motion. One example is a colloidal dispersion of micron-sized or smaller solid particles in a fluid. Just as in homogenous liquids, the mechanical properties of a colloidal dispersion depend on the mobility of their constituent particles. Unlike homogeneous liquids, however, the mobility of a colloidal dispersion is not typically controlled by temperature. Rather, it is controlled by the packing fraction, the fraction of the total fluid volume filled by the dispersed particles. As the packing fraction increases, the mobility decreases and the shear viscosity increases until the colloidal dispersion behaves macroscopically like a solid, at which point it is said to have undergone a colloidal glass transition.

Even complex fluids whose dispersed phase elements are too large to undergo Brownian motion may form a glass. The bubbles in a typical foam or the grains in a typical granular material, for instance, are much too large to undergo thermal motion. A foam or granular material is therefore far from equilibrium, and its state depends sensitively on how it is prepared. Under most preparations, such a system is disordered. It is also a solid, because it can only flow if subjected to

3

sufficient mechanical stress to overcome the surface tension or friction holding it in its configuration. However, if such a mechanical stress is applied and maintained, a foam or granular material typically settles into a nonequilibrium steady state.

Liu and Nagel proposed to organize such nonequilibrium steady states alongside supercooled liquids and colloidal glass-formers in a "jamming phase diagram" parameterized by temperature, packing fraction, and applied stress [70]. Many systems can be perturbed along two or three of these axes. For instance, a glass-forming liquid may be sheared as well as heated, while a sheared a granular material may be vibrated to provide random energy similar to heat. Since most glass-forming systems jam as packing fraction increases, temperature decreases, and/or applied stress decreases, Liu and Nagel suggested that some universal features of glass-forming systems may be understood in terms of a jamming phase diagram that partitions the three-dimensional parameter space into two phases, a glass, or jammed, phase and a fluid phase, separated by a dynamical glass transition surface.

1.3 Model

In order to understand how the jamming phase diagram may explain some universal aspects of glass and the glass transition, it is valuable to investigate a theoretical model that isolates the minimal ingredients necessary to produce a glass. In this work, we consider disordered collections of spheres in three dimensions or disks in two dimensions. We promote disorder by using bidisperse spheres, half with diameter d and half with diameter $1.4d$. Both species have mass m. The

spheres interact through a finite-range pairwise additive interaction potential. We consider both the hard-sphere potential

$$V_{\text{HS}}(\vec{r}_{ij}) = \begin{cases} \infty, & r_{ij} < d_{ij} \\ 0, & r_{ij} \geq d_{ij} \end{cases} \tag{1.1}$$

and a class of soft-sphere potentials

$$V_\alpha(\vec{r}_{ij}) = \begin{cases} \dfrac{\epsilon}{\alpha} \left(1 - \dfrac{r_{ij}}{d_{ij}}\right)^\alpha, & r_{ij} < d_{ij} \\ 0, & r_{ij} \geq d_{ij} \end{cases} \tag{1.2}$$

where $d_{ij} = (d_i + d_j)/2$ is the separation at contact, ϵ is an energy scale, and α is the exponent parameterizing the shape of the interaction. Notice that the hard-sphere potential may be thought of as the $\alpha = 0$ limit of the soft-sphere potential. Throughout the rest of this work, we will often present results in units such that $\epsilon = d = m = 1$, although we will sometime retain the model parameters for clarity. We will always present temperatures in units with the Boltzmann constant k_B set equal to 1.

Such a simple model displays much of the rich behavior of various systems that jam or undergo glass transitions. The model with $\alpha = 2$ was original developed as a "bubble model" to describe foams [29, 30]. Since thermal motion is irrelevant for foams made up of macroscopic bubbles, the relevant control parameters are packing fraction and applied stress. If the packing fraction ϕ of the spheres is set greater than random close packing ($\phi_c \approx 0.64$ in three dimensions or $\phi_c \approx 0.84$ in two dimensions), it behaves like a solid foam, with a finite pressure and shear

5

modulus. Like a foam, it can be made to flow by continuously shearing it. If some mechanism for energy dissipation is provided, the sheared system will settle down to a nonequilibrium steady state with a well-defined average shear stress σ. To model foam bubbles with insignificant inertia, the bubble model uses overdamped dynamics, but similar models include inertia to model granular materials. The shear rheology–that is, the dependence of shear stress on strain rate–of the bubble model agrees with that of a real foam: at low shear strain rates the shear stress is roughly uniform, exhibiting a dynamic yield stress, while at higher strain rates the shear stress increases. Since the relaxation time is controlled by the inverse strain rate, we may think of this shear-rate-dependence as a dynamic glass transition controlled by the applied stress rather than the temperature. If the applied stress is less than the dynamic yield stress, the foam behaves like a solid. As the applied stress increases beyond the dynamic yield stress, the foam behaves like a fluid with a relaxation time that decreases with increasing applied stress.

Just like a real foam, the bubble model also loses its solid-like character as the packing fraction decreases, that is, as the foam becomes increasingly wet: both the shear modulus and dynamic yield stress vanish continuously as $\phi \rightarrow \phi_c$ from above [29, 30, 80]. This loss of rigidity has been shown to have a universal character in the sense that the exponents governing the vanishing of a number of static quantities like the shear modulus, the pressure, the bulk modulus, and the coordination number (the average number of contacts) can be written as simple functions of the interaction exponent α [79]. Whether this holds for dynamic quantities like the dynamic yield stress is still an active subject of research [80, 45, 83].

By also varying the third parameter of the jamming phase diagram, temperature, the sphere model becomes a model for a colloidal or molecular glass-forming liquid. At high packing fractions $\phi > \phi_c$ and zero applied shear stress, the model behaves like a fragile glass former: the relaxation time τ and shear viscosity η increase faster than exponentially with inverse temperature as temperature decreases toward a dynamic glass transition temperature. Just as in experiments, the dynamic glass transition of the model depends on how long of a simulation we are willing to conduct in order to measure the relaxation time; we define the dynamic glass transition as the temperature at which τ equals some large but arbitrary value. If, instead, we fix the temperature and vary the packing fraction, the model behaves like a colloidal glass-forming liquid: the relaxation time and viscosity increase rapidly with packing fraction as the packing fraction increases toward a colloidal glass transition packing fraction. By shearing the system while holding the temperature constant, the model behaves like a soft glassy material or a conventional glass-forming liquid near its glass transition: it flows with a well-defined steady-state shear stress σ. Like for sheared glass, the flow is shear-thinning: the shear viscosity $\eta = \sigma/\dot{\gamma}$ decreases with increasing shear strain rate $\dot{\gamma}$.

1.4   Outline

In chapter 2 we will demonstrate that the jamming phase diagram is universal for the class of sphere models in a particular limit. In particular, we will show that the dynamics of the class of soft sphere models with various exponents α collapse

onto the dynamics of the hard sphere model [110, 49]. This result is nontrivial because the definition of the glass transition for soft spheres relies on there being an energy scale in the problem. The glass transition is the temperature at which the relaxation time becomes too large to measure; for instance, the temperature at which the shear stress correlation function no longer relaxes and the system acquires a static shear modulus. Both the glass transition temperature and the shear modulus acquire their energy scales from the interaction energy ϵ of Eq. 2.10. For hard spheres, there is no interaction energy to set the glass transition temperature or the shear modulus. However, we find that we can collapse the soft sphere models onto the hard sphere model by considering energies and energy densities in relation to the pressure rather than in absolute terms. Using the correct choice of units [110], hard spheres become the low-pressure limit of soft spheres. Decreasing pressure and increasing the hardness of spheres are mathematically equivalent: both cause collisions to be faster and less penetrating. Remarkably, the crossover from solid to liquid behavior as a function of temperature remains qualitatively unchanged as we take this low-pressure limit. Even for hard spheres, the temperature controls the glass transition, but only in relation to the pressure. In the hard sphere limit, the entire phenomenology of the glass transition is mediated by a single thermodynamic parameter, the ratio T/p of temperature to pressure. This ratio determines how much volume thermal fluctuations open up by doing work against the pressure. Extending the glass transition along the applied stress axis of the jamming phase diagram, we find that the glass transition is controlled by two ratios: T/p and the ratio σ/p of applied shear stress to pressure. The data collapse in the low pressure limit suggests that the glass transition may be

controlled by these two geometric quantities for a wide range of systems without regard to the details of their interactions.

In chapter 3 we will investigate to what extent the nonequilibrium axis of the jamming phase diagram, applied stress, behaves like the equilibrium axes. At finite shear stress, the system is out of equilibrium, so we may not necessarily employ statistical mechanics to determine material properties in terms of thermodynamic quantities like temperature and pressure. Indeed, such thermodynamic quantities are not even well defined. Different expressions that equal the temperature in equilibrium yield different values for steadily sheared spheres. However, recent simulations of soft sphere glass have shown that many different measurements of temperature fall into two classes [10, 11, 12, 27, 54, 72, 78, 81]. Measurements of the first class reflect high-frequency fluctuations and yield the temperature of the thermal bath, while measurements of the second class reflect low-frequency fluctuations and yield a different value that is consistent within the class of measurements. This different–in general higher–temperature is termed the effective temperature. We find that the effective temperature influences material properties of the model in a similar way that the bath temperature controls material properties in the absence of applied stress [48, 46]. The effective temperature always stays above a glass transition effective temperature similar to the glass transition temperature found without shear. This implies that in order for the sphere model to flow, the low-frequency fluctuations must exceed a threshold value, regardless of whether the flow is induced by thermal fluctuations or applied stress. By demonstrating the validity of the effective temperature concept for hard spheres, we show that in the low-pressure limit, this threshold value is

simply set by the pressure. Moreover, we find that the dynamics of the fluid, even well above threshold, are largely controlled by the effective temperature and are not separately controlled by the kinetic temperature. This suggests that over a wide range of parameter space, the mechanism for fluidization is similar regardless of whether the low frequency fluctuations are caused by temperature or applied stress.

Finally, in chapter 4 we will investigate in more microscopic detail why the dynamics slow down so dramatically near the glass transition. Since the glass transition is associated with few changes in static structure, we must look at dynamical quantities to find the correlations responsible for the slowing down. We find these correlations using a dynamic susceptibility that measures fluctuations in the number of mobile particles [5, 14, 15, 16, 26, 40, 88]. Since mobility is defined in terms of a length scale and a time scale, the dynamic susceptibility is a function of these two scales. By measuring the dynamic susceptibility as a function of both parameters, we discover that large correlations in the dynamics are a more general feature than previously appreciated [47]. In agreement with previous work, we find a maximum in the dynamic susceptibility associated with the onset of diffusive motion, a process that becomes increasingly slow and cooperative as the temperature decreases toward the glass transition temperature. In addition, we find a secondary maximum at much earlier times associated with the initial trapping of spheres in cages formed by their neighbors. Our results suggest that such correlated, or heterogeneous, dynamics must in fact be general features of crossovers in the dynamics from one type of motion to another type of motion. In order to understand the glass transition, we must focus on the crossover

associated with the dynamic transition from solid-like response at short times to fluid-like response at long times, that is, the crossover from caged motion to diffusive motion. By examining the temperature-dependence of this "cage-escaping" maximum in the dynamic susceptibility, we find that slow dynamics appear to be due to an exponential dependence of the relaxation time on the number of spheres moving in a correlated manner. This exponential dependence lends credence to theories of the glass transition involving cooperative-rearranging regions [102].

Chapter 2

Jamming Phase Diagram

2.1 Introduction

A wide variety of fluids form glasses along a variety of routes. In all cases the relaxation time of the fluid increases as a control parameter is varied until it can no longer be measured, at which point the system becomes a solid on the time scale of the measurement. Homogeneous liquids form conventional glasses as temperature decreases [31], while complex fluids such as colloids, foams, and emulsions form "soft glasses" as the packing fraction of the dispersed phase increases [21]. Near the glass transition, both types of glasses can also be fluidized by applying some external load such as shear stress. For this reason, Liu and Nagel proposed to organize a variety of glass-forming fluids in a "jamming phase diagram" parameterized by temperature, packing fraction, and applied stress [70]. In this diagram, glassy or jammed states at low temperature, high packing fraction, and low applied stress are separated from fluid states at high temperature, low pack-

ing fraction, and/or high applied stress by a surface of dynamical glass transitions defined by some large but arbitrary value of the relaxation time.

The utility of the jamming phase diagram lies in its ability to capture universal features of glassy dynamics independent of specific details of glassy systems. We establish this utility by analyzing the dependence of relaxation time on the three independent control parameters of the jamming phase diagram for a class of model glass-forming liquids. In the limit of low pressure and temperature, we can scale the relaxation time onto a function of just two parameters, the ratio T/p of temperature to pressure and the ratio σ/p of shear stress to pressure, independent of both the third independent control parameter and the model parameters.

In section 2.2, we focus on the jamming phase diagram restricted to the equilibrium plane at zero applied stress. Along this plane, the temperature-driven glass transition is equivalent to the density-driven colloidal glass transition in the limit of low pressure [110]. In section 2.3, we consider nonzero applied stress to establish a jamming phase diagram that is a universal function of just two control parameters, T/p and σ/p, in the low-pressure limit [49].

2.2 Universal Glass Transition in the Hard-Sphere Limit

The universality of the jamming phase diagram at zero applied stress and low pressure was established by Ning Xu et al [110]. For completeness, we recap these results before moving onto the jamming phase diagram at finite stress in section 2.3.

We consider the class of models introduced in section 1.3, a bidisperse collection of spheres of mass m, half with diameter d and half with diameter $1.4d$. The spheres interact through pairwise additive interaction potentials $V(r_{ij})$. The spheres do not interact at large separations: $V(r_{ij}) = 0$ for $r_{ij} \geq d_{ij}$, where $d_{ij} = (d_i + d_j)/2$ is the separation at contact. If $r_{ij} < d_{ij}$, the spheres repel each other through one of several central-force potentials. In addition to the hard sphere potential

$$V_{\text{HS}}(r_{ij}) = \infty \tag{2.1}$$

and the class of soft-sphere potentials

$$V_\alpha(r_{ij}) = \frac{\epsilon}{\alpha} \left(1 - \frac{r_{ij}}{d_{ij}} \right)^\alpha \tag{2.2}$$

of section 1.3, we also consider the Weeks-Chandler-Anderson potential [106]

$$V_{\text{WCA}}(r_{ij}) = \frac{\epsilon}{72} \left(\left(\frac{d_{ij}}{r_{ij}} \right)^{12} - 2 \left(\frac{d_{ij}}{r_{ij}} \right)^6 + 1 \right). \tag{2.3}$$

We use units such that the energy scale ϵ, the sphere mass m, and the small sphere diameter d are set equal to 1. Notice that the hard-sphere potential may be thought of as the $\alpha = 0$ limit of the soft-sphere potential. Among the class of soft sphere models, we use a harmonic repulsion ($\alpha = 2$) and a Hertzian repulsion ($\alpha = 5/2$).

We determine the relaxation time of the models as a function of temperature T and pressure p by conducting molecular dynamics simulations of $N = 1000$ spheres with periodic boundary conditions. For the hard sphere system, we use an event-

driven simulation at fixed volume and energy. For the soft potential system, we use a molecular dynamics simulation at constant temperature and pressure. We define the relaxation time from the relaxation of density fluctuations. We calculate the self-part of the intermediate structure factor: $S(\vec{k}, t) = \frac{2}{N} \sum_i \exp(i\vec{k} \cdot [\vec{r}_i(t) - \vec{r}_i(0)])$ [61], where the sum is over all large particles, $\vec{r}_i(t)$ is the location of particle i at time t, and $\vec{k}$ is chosen in the $x-$direction. The amplitude of $\vec{k}$ satisfies the periodic boundary conditions and is approximately the value at the first peak of the static structure factor. We define the relaxation time τ to be the time at which $S(\vec{k}, \tau) = e^{-1} S(\vec{k}, 0)$. We take data after a system has been equilibrated for several τ.

Fig. 2.1(a) shows the relaxation time τ versus temperature T for a system with harmonic repulsions ($\alpha = 2$ in Eq. 2.10) that is cooled at different fixed low pressures, p. This corresponds to the standard trajectory for experiments on supercooled liquids undergoing the glass transition, a trajectory in which p is typically fixed at atmospheric pressure. Fig. 2.1(b) shows τ versus $1/p$ at different fixed T for the same system; in these trajectories, we raise p at fixed T as is typically done in experiments on colloidal systems. As expected, τ increases with decreasing T and increasing p.

Fig. 2.2(a) shows that we can collapse the data in Fig. 2.1 for *all* the trajectories, both at fixed pressure and fixed temperature, onto a single curve by scaling the relaxation time by $\sqrt{m/pd}$ and temperature by pd^3, so that

$$\frac{\tau}{\sqrt{m/pd}} = F\left(\frac{T}{pd^3}\right). \tag{2.4}$$

15
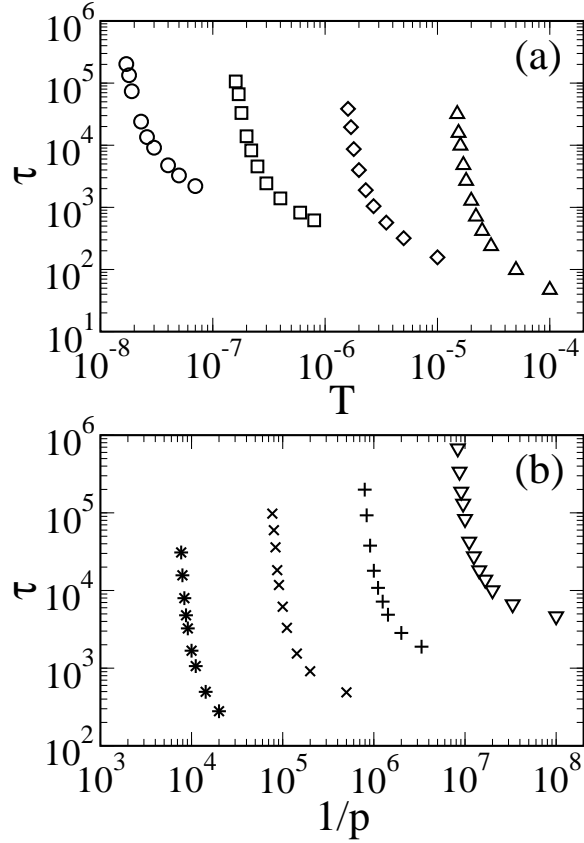
Figure 2.1: Relaxation time versus different control parameters for a system of 1000 particles with harmonic repulsions. (a) Relaxation time τ versus temperature T at different fixed pressures, p : $p = 2 \times 10^{-7}$ (circles), $p = 2 \times 10^{-6}$ (squares), $p = 2 \times 10^{-5}$ (diamonds), and $p = 2 \times 10^{-4}$ (upward triangles). (b) Relaxation time τ versus inverse pressure $1/p$ at different fixed temperatures: $T = 10^{-8}$ (downward triangles), $T = 10^{-7}$ (pluses), $T = 10^{-6}$ (crosses), and $T = 10^{-5}$ (stars).

This collapses data ranging over 4 decades of temperature and pressure by using the time scale $\sqrt{m/pd}$ and energy scale pd^3 to make relaxation time and temperature dimensionless [25]. The characteristic time $\sqrt{m/pd}$ is proportional to the time for a particle starting at rest to move its diameter d due to a pressure p and is the duration of a pressure-driven particle rearrangement. The depen-
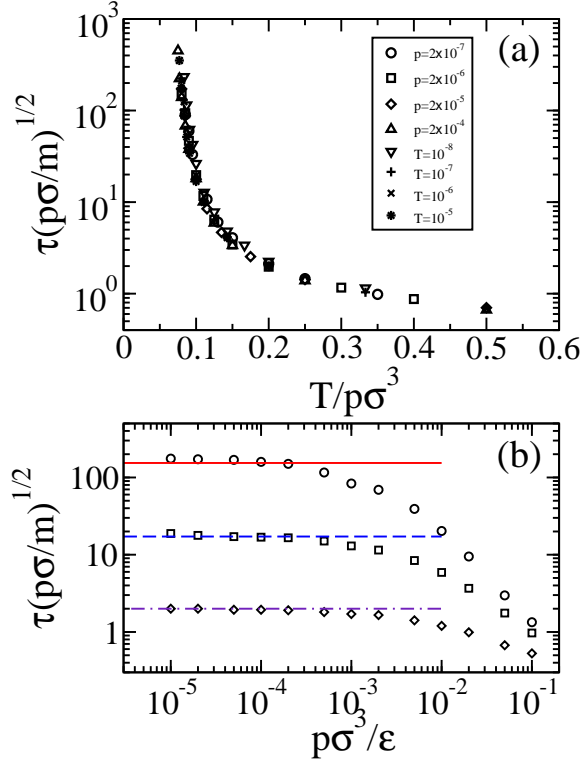
Figure 2.2: Collapse of all the relaxation time data shown in Fig. 2.1. (a) Scaled relaxation time, $\tau/\sqrt{m/pd}$, versus scaled temperature T/pd^3. (b) Scaled relaxation time $\tau/\sqrt{m/pd}$ versus scaled pressure pd^3/ϵ, for $T/pd^3 = 0.08$ (circles), $T/pd^3 = 0.1$ (squares) and $T/pd^3 = 0.2$ (diamonds). Horizontal lines show the limiting values of $\tau\sqrt{pd/m}$ as $pd^3/\epsilon \to 0$.

dence on T/pd^3 implies that both T and p are equally important in controlling the dimensionless relaxation time.

Dimensional analysis provides a starting point for understanding the implications of the data collapse of Eq. 2.4. The dimensionless time $\tau/\sqrt{m/pd}$ can be written as a function of the dimensionless variables of the system. In addition to T/pd^3, another dimensionless ratio is pd^3/ϵ, where ϵ sets the scale of the interaction energy in Eq. 2.10. There are no other independent dimensionless variables

for the system with harmonic repulsions. The dimensionless relaxation time must therefore satisfy

$$\tau\sqrt{\frac{pd}{m}} = f\left(\frac{T}{pd^3}, \frac{pd^3}{\epsilon}\right). \tag{2.5}$$

The data shown in Fig. 2.2(a) all lie at low pressures, where the second argument in Eq. 2.5, pd^3/ϵ, is small. In Fig. 2.2(b), we show the scaled relaxation time versus pd^3/ϵ at three values of T/pd^3. In all cases, the data approach an asymptotic value at low pd^3/ϵ. Thus, in the low-pd^3/ϵ limit, $\tau\sqrt{pd/m}$ is a function of T/pd^3 only, consistent with the collapse of Fig. 2.2(a).

The limit $pd^3/\epsilon \to 0$ is always satisfied in the hard-sphere limit, $\epsilon \to \infty$. Thus, the relaxation time for hard spheres should collapse onto the same scaling form as in Fig. 2.2. Moreover, all potentials that behave as hard spheres in the low-pressure limit by preventing overlap between particles—namely, all potentials with finite-ranged repulsions–should also collapse onto the same form at low pd^3/ϵ. This is not what we would expect from dimensional analysis alone, since different potentials can contain additional dimensionless parameters, such as the exponent α in Eq. 2.10. However, the physics of the $pd^3/\epsilon \to 0$, hard-sphere limit suggests that collapse should occur, irrespective of the value of α, as long as $\alpha \geq 0$ so that the potential is repulsive.

This is corroborated in Fig. 2.3, where we show the data of Figs. 2.1 and 2.2 for harmonic repulsions ($\alpha = 2$ in Eq. 2.10) together with data for three other potentials: Hertzian repulsions ($\alpha = 5/2$ in Eq. 2.10), the hard-sphere potential (Eq. 2.9), and the Weeks-Chandler-Andersen potential (Eq. 2.3). Indeed, all of these systems collapse onto the *same scaling form*. Thus, for the low-pressure (low

18
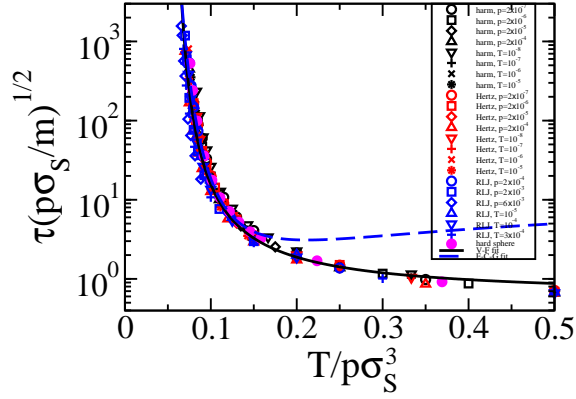
Figure 2.3: Scaled relaxation time, $\tau/\sqrt{m/pd}$, versus scaled temperature T/pd^3 for all the data for the harmonic potential (black) in Fig. 2.1 as well as for the Hertzian potential, $\alpha = 5/2$ (red), the hard-sphere potential (magenta), and the Weeks-Chandler-Andersen potential (blue). Black solid curve is the Vogel-Fulcher fit: $y = 0.59 \exp(0.18/(x - 0.045))$, where $y = \tau/\sqrt{m/pd}$ and $x = T/pd^3$. Blue-dashed curve is a fit to the Elmatad-Chandler-Garrahan form: $y = 3.1 \exp[0.064(x^{-1} - 4.72)^2]$.

pd^3/ϵ) data considered here, $\tau\sqrt{pd/m}$ is a function of T/pd^3 only and does not depend separately on the interaction potential - either on its form (*i.e.*, whether it is given by Eq. 2.9, Eq. 2.10 with different exponents α, or Eq. 2.3) or on its overall magnitude, ϵ. This represents a major simplification of the relaxation-time data.

While the scaled dynamics are independent of dimensionless parameters characterizing the inter-particle potential, they may be affected by other dimensionless numbers characterizing the system. For example, relaxation time data for hard-sphere systems with different polydispersities or diameter ratios will not necessarily collapse.

The data collapse suggests a way of looking at the glass transition in this limit

where the relaxation time is only a function of T/pd^3. The ratio of T/p corresponds to an effective volume created by using thermal energy to do work against the pressure: $p\Delta V \sim T$. In the hard-sphere glass transition, the system relaxes via free volume. Likewise, soft-sphere liquids can create free volume by using thermal energy. At high temperatures, where there is plenty of this "thermal" free volume, the system relaxes rapidly; at low temperatures, where there is less thermal free volume, the system relaxes more slowly.

The form of the scaling function, $F(x)$, shown in Fig. 2.3, should tell us whether the system has a thermodynamic glass transition. If such a transition exists, as has been suggested theoretically for hard spheres [84], then $F(x)$ should diverge at a nonzero value of T/pd^3, $i.e.$, at nonzero T for soft-sphere liquids or at finite p for hard spheres. Fig. 2.3 shows that over the dynamic range of our simulations, the Vogel-Fulcher form,

$$\tau\sqrt{\frac{pd}{m}} = C\exp\left(\frac{A}{x-x_0}\right) \tag{2.6}$$

with $x = T/pd^3$, provides a reasonable fit (solid line) with $x_0 = 0.045$, $A = 0.18$ and $C = 0.59$. The scaling collapse and Eq. 2.6 imply that $T_0/pd^3 = x_0$ so that $T_0 = pd^3 x_0$. In other words, T_0 increases with pressure. These results are consistent with recent numerical studies on spheres with harmonic repulsions [17], which show that T_0 increases with packing fraction above some critical value. The fit in Eq. 2.6 corresponds to a strength index $A/x_0 = 4.0$, indicative of a fragile glass-former [18, 6].

We also find that a fitting form proposed by Elmatad, et al. [32], for which

$\tau / \sqrt{m/pd}$ diverges only at $T/pd^3 = 0$, provides an equally good fit in the regime of interest at small T/pd^3. For this fitting form,

$$\tau \sqrt{\frac{pd}{m}} = C_1 \exp \left[A_1^2 \left(\frac{1}{x} - \frac{1}{x_1} \right)^2 \right],$$

(2.7)

where $x = T/pd^3$. We find $x_1 = 0.21$, $A_1 = 0.25$ and $C_1 = 3.1$. Thus, we cannot distinguish whether the scaling function diverges at nonzero or zero T/pd^3. This is not surprising, since even experiments with 17 decades of dynamic range cannot tell whether there is a thermodynamic glass transition. However, we note that if there is no thermodynamic glass transition, the scaling function diverges at $T/pd^3 = 0$, so that the relaxation time diverges in the double limit $T/pd^3 \rightarrow 0$, $pd^3/\epsilon \rightarrow 0$. This double limit corresponds to the zero-temperature jamming transition of frictionless spheres with finite-ranged repulsions, also known as Point J [79]. This implies that the glass transition is controlled by Point J if there is no intervening thermodynamic glass transition.

The relaxation time is not the only quantity to exhibit data collapse in the low pd^3/ϵ limit. Other quantities, including those such as the packing fraction, ϕ, that are independent of the dynamics, should also exhibit collapse in that limit. The packing fraction is the number density made dimensionless by the average particle volume. For a fixed potential, ϕ must be expressible as a function of T/pd^3 and pd^3/ϵ. In the low-pressure, hard-sphere limit where $pd^3/\epsilon \ll 1$, it should satisfy $\phi = \tilde{H}(T/pd^3)$ with the same scaling function $\tilde{H}(x)$ for all finite-ranged repulsive
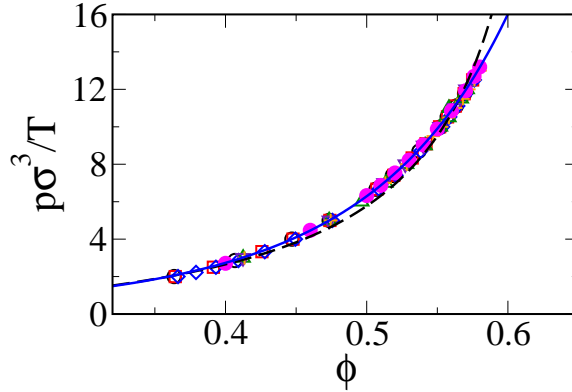
Figure 2.4: Equation of state at low pd^3/ϵ for hard sphere systems (solid magenta circles) and systems with harmonic repulsions measured along both constant temperature and constant pressure trajectories. The dashed line is a fit to free-volume theory, $pd^3/T = 0.98\phi/(1 - (\phi/\phi_c)^{1/3})$, with $\phi_c = 0.66$. The solid line is an empirical fit given by $pd^3/T = \phi/(1 - (\phi/1.13))^{4.35}$.

potentials. This function can be inverted to yield the equation of state

$$\frac{pd^3}{T} = H(\phi). \tag{2.8}$$

Fig. 2.4 shows the data collapse for the equation of state along different trajectories and for different potentials for our bi-disperse systems in three dimensions. We have shown two fits to the data. The dashed line is a fit to free volume theory for ϕ near the fitting parameter $\phi_c = 0.66$. This form fits experimental data for colloidal hard spheres and numerical data for hard spheres reasonably well [57], but is clearly unsatisfactory here. The solid line is an empirical fit to the data (see caption).

Our results show that the data for the relaxation time in many different systems collapse onto a single curve of $\tau\sqrt{pd/m}$ versus T/pd^3. This collapse, how-

ever, is confined to $p \ll \epsilon/d^3$. We find that upon increasing the pressure, there are deviations from the scaling collapse (see Fig. 2.2(b)). This implies that there are additional contributions to relaxation near the glass transition, beyond the particle rearrangements facilitated by the thermal free volume. At large pd^3/ϵ, relaxation also occurs because thermal fluctuations drive the system across energy barriers. This contribution can be accounted for by introducing an effective hard-sphere radius following a modified Barker-Henderson procedure [9] that uses the pair distribution function [90].

The relative effects of T and p on τ in glass-forming liquids have been studied experimentally, with differing conclusions [2, 100, 107]. In order to understand the consequences for molecular liquids, we must first understand the corrections to the leading hard-sphere behavior when pd^3/ϵ is no longer small. Molecular liquids typically lie at densities above the jamming transition. They also have long-ranged attractions as well as the short-ranged repulsions considered here. For these glass-forming liquids, hard spheres may still be a useful starting point, but at least one other distinct contribution to the relaxation must also be considered.

2.3 Universal Jamming Phase Diagram in the Hard-Sphere Limit

Many disordered solids can be made to flow by some combination of increasing temperature, decreasing density, and applying a mechanical load [70]. The most apparent examples are complex fluids, heterogeneous two-component mixtures such as foams [52], emulsions [75], colloidal dispersions [22, 85], and granular

materials [38]. Even though one or both of the constituent phases are fluids, complex fluids behave macroscopically like solids when the packing fraction of the dispersed phase is large enough. However, they are "soft glasses" because they can be fluidized by applying a sufficiently large mechanical load such as a shear stress. Complex fluids are influenced by thermal fluctuations to a greater or lesser degree depending on the size of the bubbles, droplets, or grains comprising the dispersed phase. While the glass transition for homogeneous liquids is most typically controlled by temperature, many conventional glass-forming liquids show strong sensitivity to pressure, shear stress, or both. The glass transition temperature of molecular glass-forming liquids tend to increase with pressure [89, 107]. While conventional glasses tend to be more brittle than their soft counterparts, at temperatures near the glass transition, "hard" glasses also become soft: their shear viscosities may be reduced by applying large shear stresses. Such shear thinning appears to be a general feature of molecular and atomic glass-formers near their glass transitions, having been observed in oxide [105, 104], molecular [112], and metallic [71] glasses.

Given the ubiquity of such soft, glassy response among both "soft" and "hard" glasses, we may ask whether universal mechanisms account for the similar response among glassy systems to changes in density, temperature, and shear stress. In particular, can we organize glassy materials in a "jamming phase diagram" parameterized by temperature, packing fraction, and shear stress, as proposed by Liu and Nagel [70]? In this section, we address this question for a particular class of glassy materials, models consisting of spheres with purely repulsive interactions. We show that we can orient this class of models on a three-dimesional

phase diagram parameterized by three dimensionless quantities related to density, temperature, and shear stress. Our representation is particularly useful because it defines the three-dimensional state space as the product of two orthogonal planes: an equilibrium plane spanned by temperature and packing fraction, and a hard sphere plane approached in the limit of vanishing temperature and pressure. Near the latter plane, the jamming phase diagram becomes universal, insensitive to the details of the interactions. The state point at zero temperature, zero shear stress, and vanishing particle overlap that controls the singular behavior of static sphere packings [79] lies at the origin of our new jamming phase diagram. We show that Point J is hidden behind a two-dimensional dynamic glass transition surface and explore the shape of this surface.

Our class of models are frictionless spheres with finite-range, repulsive interactions. In particular, as in section 2.2, we consider bidisperse spheres of mass m, half with diameter d and half with diameter $1.4d$. The spheres interact through pairwise additive interaction potentials $V(r_{ij})$. The spheres do not interact at large separations: $V(r_{ij}) = 0$ for $r_{ij} \geq d_{ij}$, where $d_{ij} = (d_i + d_j)/2$ is the separation at contact. If $r_{ij} < d_{ij}$, the spheres repel each other through either the hard sphere potential

$$V_{\text{HS}}(r_{ij}) = \infty \tag{2.9}$$

or one of a class of soft-sphere potentials

$$V_\alpha(r_{ij}) = \frac{\epsilon}{\alpha} \left(1 - \frac{r_{ij}}{d_{ij}} \right)^\alpha . \tag{2.10}$$

Notice that the hard-sphere potential may be thought of as the $\alpha = 0$ limit of the

soft-sphere potential.

We determine the steady-state rheology and the relaxation time of the models by conducting molecular dynamics simulations at fixed temperature T and shear strain rate $\dot{\gamma}$. We define the temperature by the velocity fluctuations relative to an imposed uniform shear gradient. The shear strain rate is imposed using Lees-Edwards boundary conditions. We use simple periodic boundary conditions in the other dimension. For the hard spheres, we use an event-driven algorithm [55, 74] at fixed packing fraction ϕ. We periodically rescale the velocities in order to keep the temperature within 1% of the desired value. For the soft spheres, we use a conventional molecular dynamics algorithm that numerically integrates classical equations of motion. We employ Gaussian constraints [33, 34, 53] to fix the instantaneous temperature T and pressure p. Details of our algorithms may be found in appendix A. We characterize the rheology in terms of the steady-state shear stress σ. We define the relaxation time τ as the time for spheres to diffuse on average a distance of one small diameter. To exclude the direct effect of the uniform shear, we define τ in terms of the root mean square displacement in the vorticity direction, $\Delta r_z(t) = \sqrt{\langle (r_z(t) - r_z(0))^2 \rangle}$, as $\Delta r_z(\tau) = 1/\sqrt{3}$.

As we showed in section 2.2, it is useful to analyze the relaxational dynamics in terms of dimensionless quantities [110]. In section 2.2, we found that the dynamic glass transition of soft spheres is controlled only by the ratio of temperature to pressure, T/pd^3, in the hard sphere limit of $T \to 0$, $p \to 0$. In order to collapse the relaxation time data as a function of T/pd^3 over a range of temperatures and pressures, we scale the relaxation time by the time scale, $\sqrt{m/pd}$, which is proportional to the time for a sphere to move a distance equal to its diameter when

accelerated by a typical compressive force at pressure p. We found that corrections to the hard sphere limit are controlled by a second dimensionless group, pd^3/ϵ, which parameterizes the amount of overlap.

In order to extend this scaling to the shear stress axes, we must non-dimensionalize the shear stress σ and the strain rate $\dot{\gamma}$. As for the equilibrium relaxational dynamics, there is more than one way to do this. We choose to scale both quantities by powers of the pressure. This keeps the dependence on the interaction energy only in the dimensionless pressure, pd^3/ϵ, and results in a dimensionless shear stress σ/p and a dimensionless strain rate $\dot{\gamma}\sqrt{m/pd}$ familiar to the granular materials community [25, 38, 86]. The dimensionless shear stress is a macroscopic dynamic friction coefficient, while the strain rate is made dimensionless using the same time scale $\sqrt{m/pd}$ we used to scale the relaxation time. As the system is sheared at constant pressure, it repeatedly dilates and contracts. The dimensionless strain rate describes how fast the system is sheared relative to the time it takes for pressure to drive a dilated configuration into a close-packed configuration; it is the ratio of the contraction time to the shear time.

In Fig. 2.5, we demonstrate that the rheology for spheres with harmonic ($\alpha = 2$) interactions collapses in the low-pressure limit onto the rheology for hard spheres. In Fig. 2.5 (a), we show the unscaled rheology, shear stress vs strain rate. In the figures, we present data in units defined by setting the model parameters $m = d = \epsilon = 1$. We show data for harmonic spheres at four different pressures, $p = 10^{-4}$, $p = 10^{-3.5}$, $p = 10^{-3}$, and $p = 10^{-2.5}$, and two different dimensionless temperatures, $T/p = 0.03$ and $T/p = 0.1$. In Fig. 2.5 (b), we show that for each value of T/p we can collapse the data from the four different pressures onto the
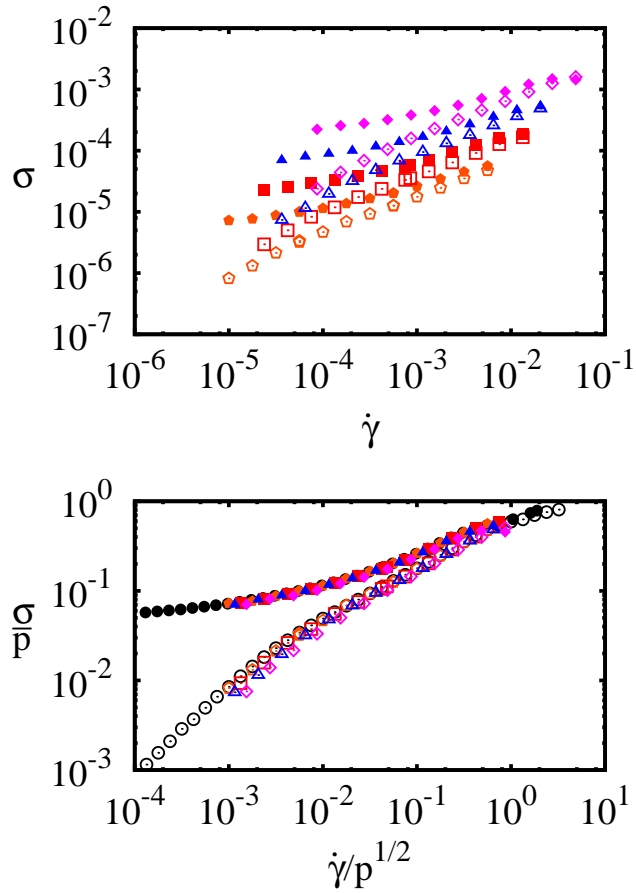
Figure 2.5: (a) Shear stress σ vs. strain rate $\dot{\gamma}$ for $\alpha = 2$, two different values of T/p, and four different values of p. The filled symbols represent $T/p = 0.03$, while the open symbols represent $T/p = 0.1$. Filled pink diamonds are $p = 10^{-2.5}, T/p = 0.03$; filled blue triangles are $p = 10^{-3}, T/p = 0.03$; filled red squares are $p = 10^{-3.5}, T/p = 0.03$; filled orange pentagons are $p = 10^{-4}, T/p = 0.03$; open pink diamonds are $p = 10^{-2.5}, T/p = 0.1$; open blue triangles are $p = 10^{-3}, T/p = 0.1$; open red squares are $p = 10^{-3.5}, T/p = 0.1$; open orange pentagons are $p = 10^{-4}, T/p = 0.1$. (b) Same data, made dimensionless by the pressure to collapse onto the hard sphere rheology. For comparison, the dimensionless shear stress vs dimensionless strain rate for hard spheres is also plotted. Black filled circles are $T/p = 0.03$, while black open circles are $T/p = 0.1$.

hard sphere curve by dividing the shear stress by the pressure and multiplying the strain rate by the time scale $\sqrt{m/pd}$. All the data at the lower dimensionless temperature, $T/p = 0.03$, collapse onto a hard sphere curve with an apparent dynamic yield stress at low strain rates, while all the data at the higher dimensionless temperature, $T/p = 0.1$, collapse onto a hard sphere curve with a linear viscous response, $\sigma/p \propto \dot{\gamma}/\sqrt{p}$, at low strain rates. At higher strain rates, the system shear thins: the dimensionless shear stress grows slower than linearly with increasing dimensionless strain rate.

For a given potential, we can understand the data collapse from dimensional analysis. If we keep all model parameters such as $\alpha = 2$ fixed, we may write the dependence of the shear stress on the three control parameters, T, p, and $\dot{\gamma}$, as a dimensionless function g of three independent dimensionless control parameters. One choice of such parameters results in the expression

$$\frac{\sigma}{p} = g\left(\frac{T}{pd^3}, \dot{\gamma}\sqrt{\frac{m}{pd}}, \frac{pd^3}{\epsilon}\right).$$

$$(2.11)$$

In the limit $p \to 0$, we expect a collapse of the form shown in Fig. 2.6,

$$\frac{\sigma}{p} = G\left(\frac{T}{pd^3}, \dot{\gamma}\sqrt{\frac{m}{pd}}\right).$$

$$(2.12)$$

As shown in Fig. 2.6 (a), the limit described by Eq. 2.12 does correspond to low pressures. At fixed T/p and $\dot{\gamma}/\sqrt{p}$, σ/p approaches a limiting value as $p \to 0$. While dimensional analysis does not require that this limit should be the same for spheres with different potentials or should equal the value for hard spheres, Fig. 2.6 shows that σ/p approaches the hard sphere value for several different

29
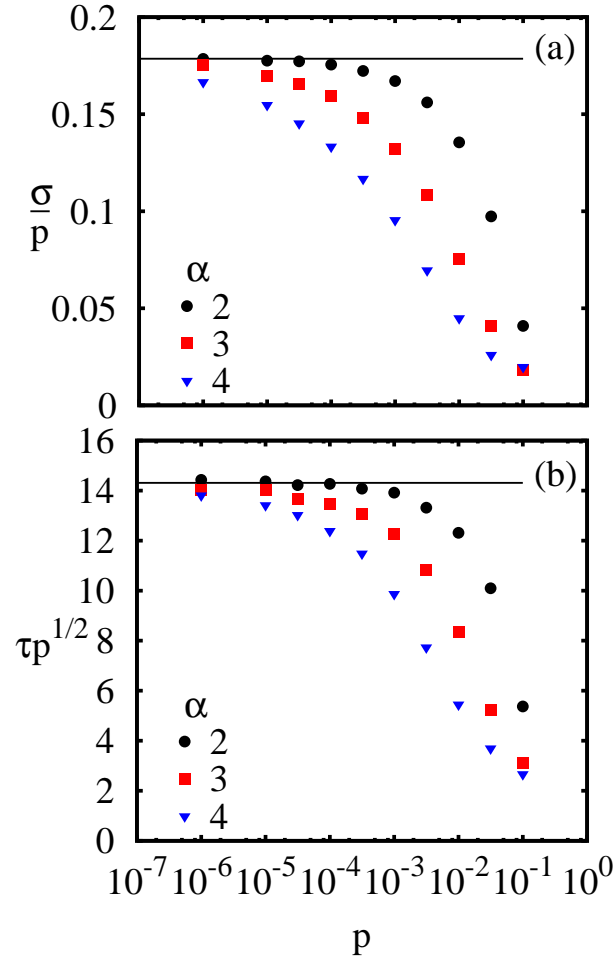
Figure 2.6: Approach to the hard sphere limit. (a) Dimensionless shear stress σ/p vs pressure p at fixed dimensionless temperature $T/p = 0.1$ and dimensionless strain rate $\dot{\gamma}/\sqrt{p} = 0.1$ for three different exponents α. (b) Dimensionless relaxation time $\tau\sqrt{p}$ vs pressure p at fixed dimensionless temperature $T/p = 0.1$ and dimensionless strain rate $\dot{\gamma}/\sqrt{p} = 0.1$ for three different exponents α. In each plot, the horizontal line represents the value for hard spheres.

exponents α as $p \to 0$. This suggests that the rheology of soft spheres with any finite-range, repulsive interactions collapses onto the rheology of hard spheres at low pressure. The data collapse is not limited to the rheology but should apply to any observable quantity as long as we non-dimensionalize it by the pressure. For instance, as we show in Fig. 2.6 (b), the dimensionless relaxation time also approaches the hard sphere value as $p \to 0$.

The data collapse of Eq. 2.12 calls for recasting the jamming phase diagram in terms of the dimensionless control parameters. Choosing a stress-controlled rather than a strain-rate-controlled parameter space, the dimensionless control parameters are T/pd^3, pd^3/ϵ, and σ/p. These parameters span the same space as T, ϕ, and σ of the original jamming phase diagram [70], but they have two advantages. First, the plane at $pd^3/\epsilon = 0$ spanned by T/pd^3 and σ/p defines the hard sphere limit. Near this plane, we have shown that the jamming phase diagram is universal for repulsive spheres in the sense that observable quantities are independent of the details of the interaction potential. The hard sphere plane is complementary to the equilibrium plane spanned by T/pd^3 and pd^3/ϵ; the full parameter space is the product of these two planes. The second advantage of the dimensionless control parameters is that Point J [79], the point at zero temperature, zero shear stress, and vanishing pressure, lies at the origin. Many elastic and structural properties of soft sphere packings approach a singular limit as Point J is approached along the pd^3/ϵ axis at $T/pd^3 = \sigma/p = 0$ [29, 30, 79, 93, 94, 108, 109].

We choose the dimensionless relaxation time $\tau\sqrt{pd/m}$ as the order parameter of our jamming phase diagram. Before constructing the jamming phase diagram, we investigate how the relaxation time relates to the rheology. Figure 2.7 shows
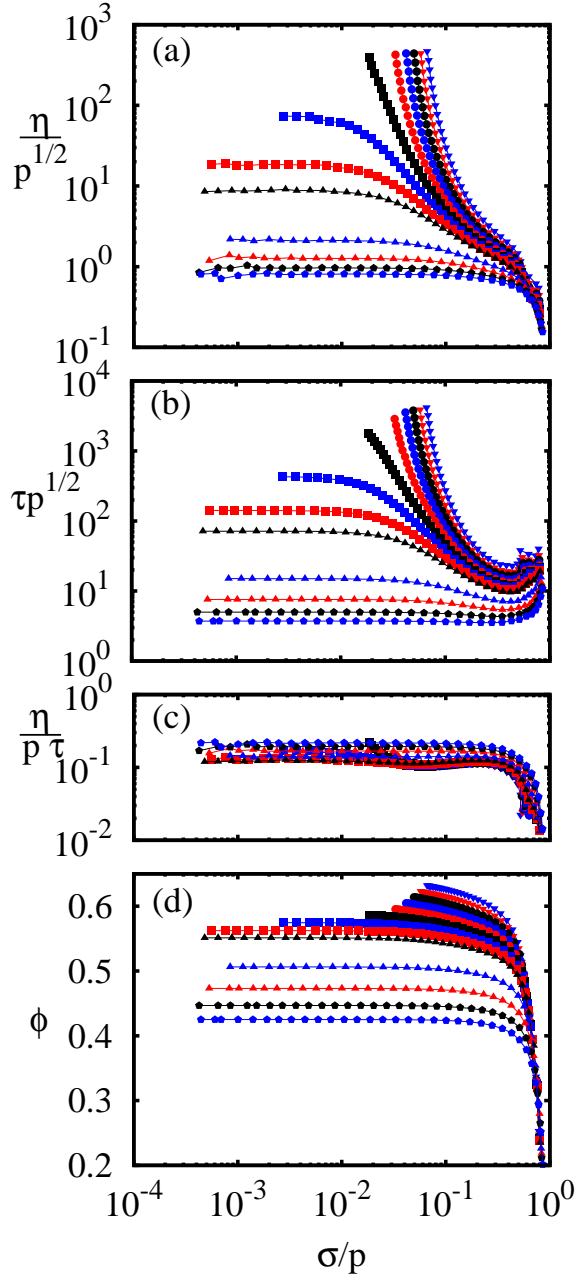
Figure 2.7: Hard sphere results interpolated at prescribed values of the dimensionless temperature T/p. (a) Dimensionless relaxation time $\tau\sqrt{p}$ vs dimensionless shear stress σ/p. (b) Dimensionless shear viscosity $\eta/\sqrt{p}$ vs σ/p. (c) Ratio of dimensionless shear viscosity to dimensionless relaxation time vs σ/p. (d) Packing fraction ϕ vs σ/p. Each connected line is a different value of T/p: 0.02 (blue down triangles), 0.03 (red down triangles), 0.04 (black circles), 0.05 (blue circles), 0.06 (red circles), 0.07 (black squares), 0.08 (blue squares), 0.09 (red squares), 0.1 (black up triangles), 0.15 (blue up triangles), 0.2 (red up triangles), 0.25 (black pentagons), and 0.3 (blue pentagons).

32

the rheology, the relaxation time, and the packing fraction for hard spheres as a function of the two dimensionless control parameters spanning the hard sphere plane, T/pd^3 and σ/p. To the best of our knowledge, no previous simulation has investigated the nonlinear rheology of hard spheres close to the glass transition. In each plot, connected lines represent fixed values of T/pd^3, while the x-axis represents σ/p. We interpolate the data at fixed T/pd^3 from simulations conducted at fixed packing fraction. In Figs. 2.7 (a) and 2.7 (b), we plot the dimensionless shear viscosity, defined as the ratio of the dimensionless shear stress to the dimensionless strain rate, and the dimensionless relaxation time. The two plots are very similar: for high temperatures, both the viscosity and the relaxation time approach limiting values at low shear stress, while for low temperatures, the viscosity and relaxation time increase without bound on the time scales available to our simulations. Indeed, the ratio of the dimensionless viscosity to the dimensionless relaxation time, plotted in fig 2.7, is insensitive to shear stress until very large shear stresses and only weakly depends on the temperature. At low or moderate shear stress, the hard sphere fluid behaves like a Maxwell fluid with a viscosity that decreases with shear stress but a modulus η/τ that remains independent of shear stress and proportional to the pressure. A shear modulus proportional to pressure has also been observed in emulsions [75] and pastes [91].

At a dimensionless shear stress of approximately 0.5, there is a dramatic change in behavior: the dimensionless relaxation time increases, and both the dimensionless shear viscosity and the packing fraction decrease more sharply than at lower shear stress. These changes are associated with the spheres layering in the plane perpendicular to the shear gradient, as indicated by long-range order in the pair

distribution function (not shown). This layering facilitates the shearing of layers relative to each other but impedes the mobility of spheres within a layer, causing the decoupling of shear viscosity and relaxation time. Such layering has been demonstrated to be an artifact of thermostats like ours that assume a linear shear profile [28, 35]. Thermostats that do not assume a linear profile yield similar results below the layering transition but do not form layers at high stresses; instead, they exhibit shear thickening, where viscosity increases with shear stress. Even with layering, our system shear thickens at fixed packing fraction, though not at fixed T/p. Since the layering is an artifact of the thermostat, we focus on the isotropic phase below $\sigma/p = 0.5$.

In Fig. 2.8, we construct the jamming phase diagram for harmonic ($\alpha = 2$) spheres. We restrict ourselves to values $T/pd^3 < 0.2$, $\sigma/p < 0.15$, and $pd^3/\epsilon < 0.2$, well separated from the layering at very high σ/p. We parameterize the jamming phase diagram by surfaces of equal dimensionless relaxation time. Since we must interpolate to find the level sets of the dimensionless relaxation time, it would be computationally expensive to construct the entire surfaces. Instead, we draw contours where the surfaces intersect four planes: the equilibrium plane at $\sigma/p = 0$, the hard sphere plane at pd^3/ϵ, a plane at $pd^3/\epsilon = 0.1$, and a plane at $pd^3/\epsilon = 0.2$. In Fig. 2.8 (a), we show sets of contours for three logarithmically spaced relaxation times, each separated by a decade. In 2.8 (b) and (c), we show contours separated by half decades for the equilibrium and hard sphere planes, respectively. The dimensionless relaxation time increases monotonically as any combination of the dimensionless control parameters are reduced, so that the contours corresponding to large dimensionless relaxation time are closest to the
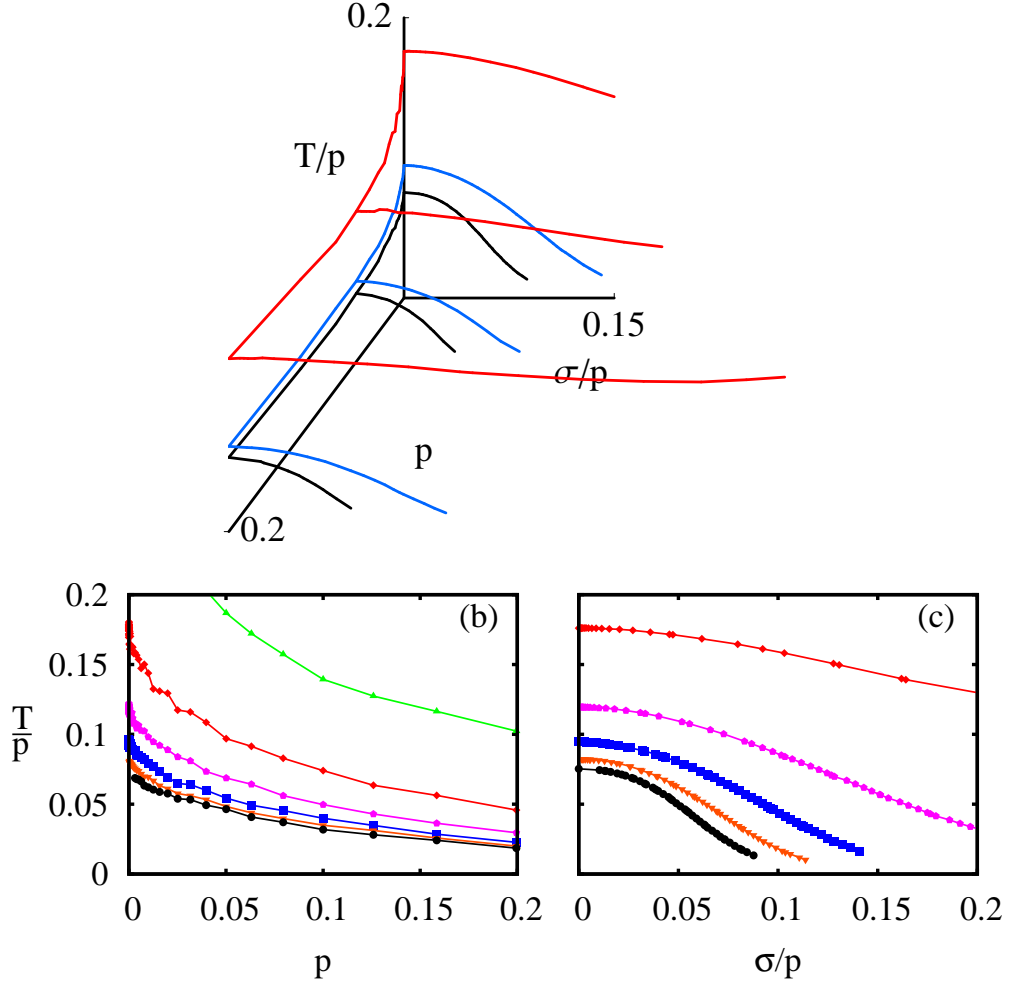
Figure 2.8: (a) Jamming phase diagram for $\alpha = 2$. Lines represent logarithmically spaced contours of equal dimensionless relaxation time (top to bottom): $\tau\sqrt{p} = 10$ (red), 10^2 (blue), and 10^3 (black). We show contour lines along four planes cut through the diagram: the equilibrium plane at $\sigma/p = 0$, the hard sphere plane at $p = 0$, a plane at $p = 0.1$, and a plane at $p = 0.2$. In (b) and (c), we show two-dimensional cuts of (b) the equilibrium plane at $\sigma/p = 0$ and (c) the hard sphere plane at $p = 0$. In (b) and (c), we show contours of equal dimensionless relaxation time spaced by half decades: $\tau\sqrt{p} = 10^{0.5}$ (yellow up triangles), 10 (red diamonds), $10^{1.5}$ (pink pentagons), 10^2 (blue squares), $10^{2.5}$ (orange down triangles), and 10^3 (black circles). The contours are constructed by interpolation.

35

origin. Notice that the contours become more closely spaced as T/p, σ/p, or p decrease. As a consequence, the relaxation time becomes too large to measure well before the system reaches Point J at $T/p = p/\sigma = p = 0$; the system undergoes a dynamic glass transition along any path approaching Point J. The dynamic glass transition forms a surface enclosing the origin.

At a given pressure, for instance $p = 0$ shown in Fig. 2.8 (c) or the constant-pressure cuts shown in Fig. 2.8 (a), the dynamic glass transition is a contour intersecting the equilibrium axis at the dynamic glass transition temperature. Below the dynamic glass transition temperature, the contour describes what may be considered either a stress-dependent dynamic glass transition temperature or a temperature-dependent dynamic yield stress. While the shape of this dynamic glass transition depends on the potential at high pressures, at sufficiently low pressures, near the hard sphere plane, the shape follows the universal form shown in Fig. 2.8 (c). At all pressures, the contours are quadratic in σ/p at small σ/p. This is expected from the symmetry of $\sigma \rightarrow -\sigma$. A similar shape has been observed for contours of equal viscosity for a model metallic glass-forming liquid [43].

We may use the jamming phase diagram to parameterize the dependence of other dimensionless observable quantities besides the relaxation time on the dimensionless control parameters. The dimensionless shear viscosity follows a similar form as the dimensionless relaxation time. The packing fraction ϕ becomes a dependent quantity in our new formulation of the jamming phase diagram. The relationship between ϕ and p at $T/p = \sigma/p = 0$ has been well studied; near Point J, the pressure is proportional to $(\phi - \phi_c)^{\alpha-1}$, where $\phi_c \approx 0.64$ is the pack-

36

ing fraction at which most static sphere packings lose mechanical stability [79]. We find that the packing fraction grows roughly linearly with $(pd^3/\epsilon)^{1/(\alpha-1)}$ away from $T/p = \sigma/p = 0$ as well. The packing fraction decreases roughly linearly with T/pd^3, consistent with the idea that T/p controls the amount of free volume. It also decreases roughly linearly with σ/p, but with a smaller coefficient, until dropping more precipitously above the layering transition near $\sigma/p = 0.5$. We emphasize that the packing fraction is a smooth function of the dimensionless control parameters everywhere in the jamming phase diagram; observed singularities in the pressure, relaxation time, and viscosity at ϕ_c [29, 30, 45, 79, 80, 83] are due to the fact that ϕ takes the value ϕ_c at the origin of our reformulated jamming phase diagram, where p, T/p, and σ/p go to zero and the relaxation time and viscosity are too large to measure.

The universality of the jamming phase diagram at low pressures allows us to understand one of the two exponents describing apparent critical scaling for soft spheres at zero temperature with damped interactions [45, 80]. References [80] and [45] examine the same class of repulsive spheres with interaction potential exponents α, but they do not couple the system to a thermal bath; instead, energy dissipates through frictional interactions. Under steady shear, the rheology of these models can be collapsed onto two branches of a master function,

$$\sigma = |\phi - \phi_c|^\beta S_\pm \left(\frac{\dot{\gamma}}{|\phi - \phi_c|^{\beta\delta}} \right), \tag{2.13}$$

where ϕ_c is a critical packing fraction. In analogy with a critical point, Eq. 2.13 suggest that the model acquires a yield stress σ_{yield} for $\phi > \phi_c$ with $\sigma_{\text{yield}} \propto$

$|\phi - \phi_c|^\beta$. While simulations show that the exponent δ depends on the precise mechanism for dissipation (overdamped vs underdamped dissipation), the exponent β appears to be insensitive to the dissipation mechanism but dependent on the interaction exponent α: $\beta = 1.2 \pm 0.1$ for $\alpha = 2$, while $\beta = 1.8 \pm 0.1$ for $\alpha = 2.5$ [45].

Shearing soft spheres with damped interactions induces velocity fluctuations that may be characterized by a granular temperature. Assuming that dissipative spheres at a strain rate $\dot{\gamma}$ and a granular temperature T behave similarly to purely elastic spheres strained at a rate $\dot{\gamma}$ and connected to a thermostat at temperature T, we can use the jamming phase diagram to understand the behavior of the dissipative models. Since temperature is not independently controlled, these models exist only on a two-dimensional surface of the jamming phase diagram. The low-$\dot{\gamma}$ limit corresponding to an apparent dynamic yield stress defines a one-dimensional curve. Such a curve must correspond to low T/p, since the granular temperature strongly depends on $\dot{\gamma}$ but the pressure does not [45]. Moreover, it must correspond to high $\tau\sqrt{p}$, since the relaxation time is proportional to $\dot{\gamma}^{-1}$ at low $\dot{\gamma}$. Combining these two observations, it is clear that the dynamic yield stress scaling corresponds to a trajectory on the jamming phase diagram near where the dynamic glass transition surface intersects the $T/p = 0$ plane. As the packing fraction is reduce toward ϕ_c, the pressure approaches 0 and the trajectory approaches the hard sphere plane. Since this trajectory is roughly perpendicular to the hard sphere plane, σ/p is constant, so $\sigma_{\text{yield}} \propto p$, consistent with Ref. [45]. Applying our observation that, to a good approximation, $pd^3/\epsilon \propto (\phi - \phi_c)^{\alpha-1}$ at low T/p and moderate σ/p, we find expect $\sigma_{\text{yield}} \propto (\phi - \phi_c)^{\alpha-1}$, in reasonable

agreement with the observed exponents $\beta = 1.2 \pm 0.1$ for $\alpha = 2$ and $\beta = 1.8 \pm 0.1$ for $\alpha = 2.5$ [45].

Our reformulation of the jamming phase diagram leads to several questions, among them the following three. First, can we understand the behavior of soft spheres in terms of hard sphere behavior for values of pd^3/ϵ beyond the universal region of the jamming phase diagram? At zero shear stress, the relaxation times of soft spheres can be collapsed onto the universal function for hard sphere using only structural information; the dimensionless relaxation time of soft spheres equals the dimensionless relaxation time of hard spheres at the same volume if their diameters are reduced following a modified Barker-Henderson procedure [9] that uses the pair distribution function [90]. Future work must determine whether such a procedure can map behavior of soft spheres at nonzero shear stress onto hard sphere behavior as well. Second, can systems with attractions be understood in terms of the jamming phase diagram? Can the axes of the jamming phase diagram be modified to take into account, for instance, the work that thermal fluctuations must do against attractions as well as external pressure? Third, how does the nonequilibrium axis, σ/p, compare or contrast with the equilibrium axes? This question will be addressed in chapter 3, where we investigate to what extent the dynamics at nonzero stress are controlled by an effective temperature.

Chapter 3

Effective Temperature

3.1 Introduction

The dynamic glass transition results when thermal fluctuations are no longer large enough to induce particle rearrangements on observable time scales. We have shown that repulsive spheres only flow when thermal fluctuations do enough work against the pressure to open up sufficient free volume. Our measurements of the jamming phase diagram for repulsive spheres reveals that another way to do work against the pressure is to apply an external shear stress. Doing so fluidizes the spheres even at temperatures well below the dynamic glass transition temperature. Shearing drives a system far from equilibrium: energy is continually supplied on long time and length scales via the boundaries and is removed on short scales by the thermal reservoir. Nonetheless, simulations show that fluctuations in such systems are well described by an effective temperature T_{eff} that is higher than the bath temperature [10, 11, 12, 54, 78], as predicted theoretically [24]. Nine

different definitions yield a common value of T_{eff} [10, 11, 12, 27, 54, 72, 78, 81], providing strong numerical evidence for the utility of the concept.

In section 3.2 we show that T_{eff} plays a critical role in fluidizing a glass [48]. We find that the shear stress collapses onto a single curve depending only on T_{eff} whenever the shear rate is high enough to dominate over thermal effects. The average inherent structure energy collapses in similar fashion. These findings suggest that T_{eff} activates particle rearrangements necessary for flow, much as thermal fluctuations do in an equilibrium liquid, supporting the idea that a common framework might describe unjamming by mechanical forcing and by temperature [70].

In section 3.3 we show how the effective temperature relates to the dimensionless jamming phase diagram we established for repulsive spheres [46]. By measuring for the first time the effective temperature for hard spheres, we focus on the portion of the jamming phase diagram spanned by the dimensionless temperature, T/pd^3, and the dimensionless shear stress, σ/p. This allows us to uncover a common mechanism for the dynamic glass transition along any path in this plane; along any trajectory, fluidization occurs on accessible time scales only if low-frequency fluctuations exceed a threshold value set by the pressure. These low frequency fluctuations are controlled by the temperature in the absence of shear but are well described by the effective temperature even far from equilibrium.

Interest in the idea of effective temperature for glass-forming liquids originated in the discovery by Cugliandolo, Kurchan, and Peliti that low-frequency fluctuations in mean-field spin glass models are described by an effective temperature different from the temperature of the environment [24]. In the low-temperature, spin-glass phase these models are out of equilibrium: while the spin correlation

function eventually decay to zero, the time scale for the decay depends on the age of the system. Time-translational invariance can be restored by steadily driving the system with an external force [13, 24] that plays a similar role as shear stress in a fluid [13]. Cugliandolo *et al* found that while the high-frequency fluctuations of such driven systems behave as if in equilibrium with the environment at temperature T, low-frequency fluctuations behave as in an equilibrium system at $T_{\text{eff}} > T$, even in the limit of vanishing drive. Specifically, a thermometer consisting of a harmonic oscillator coupled to the system reads a temperature T if the frequency of the oscillator is large but T_{eff} if the frequency is small. Moreover, the time-dependent fluctuation-dissipation relation between spin fluctuations and linear response falls into two distinct time regimes: at short times, the fluctuation dissipation theorem holds as in equilibrium, while at long times, it holds but with T replaced by T_{eff}.

While the existence of an effective temperature has been established for sheared granular matter [23, 97, 103], the establishment of the effective temperature as an observable-independent quantity characterizing the state of sheared fluids has mostly been established by simulations of simple glass-forming fluids like ours. Taken together, these simulations indicate that the low-frequency fluctuations of fluids under shear are characterized by an effective temperature whose value is consistent for several types of measurements involving several different observables. Many of the measurements derive from the fluctuation-dissipation theorem, which states that the time correlation function $C_{AB}(\tau)$ of observables A and B is related

to the associated linear response function $R_{AB}(\tau) = \partial \langle A(t+\tau) \rangle_{h_B} / \partial h_B(t)$ via

$$R_{AB}(\tau) = -\frac{1}{T} \frac{\partial C_{AB}(\tau)}{\partial \tau}. \tag{3.1}$$

The average $\langle \cdot \rangle_{h_B}$ is taken over a linearly perturbed state governed by a perturbed Hamiltonian $\mathcal{H}_{h_B}(t) = \mathcal{H}_0 - h_B(t)A$. Integrating over time, Eq. 3.1 may be rewritten in terms of the integrated response $M_{AB}(\tau) = \int_0^\tau R_{AB}(\tau')d\tau'$ as

$$M_{AB}(\tau) = \frac{1}{T} \left(C_{AB}(0) - C_{AB}(\tau) \right). \tag{3.2}$$

For out-of-equilibrium systems like sheared model glass-formers, the fluctuation-dissipation relation need not hold. However, for many observables, including displacement and Fourier components of the density, the relationship between $M_{AB}(\tau)$ and $C_{AB}(\tau)$ shows two linear regimes, one at short times with a slope $1/T$ and another at long times with a slope $1/T_{\text{eff}}$ [10, 11, 12, 78], in analogy with the observed behavior for mean-field spin glass models [24, 13]. Surprisingly, the relationship between the fluctuations and the static (infinite-time) response for a separate class of observables, including the pressure, the shear stress, and the energy, yield a consistent value of T_{eff} [81, 78], despite the fact that an effective temperature from static linear response should not agree with an effective temperature for time-dependent linear response. An effective temperature from static linear response implies that $M_{AB}(\infty) = C_{AB}(0)/T_{\text{eff}}$ in Eq. 3.2, which is inconsistent with Eq. 3.2 showing two distinct regimes with slope $1/T$ and $1/T_{\text{eff}}$ [78]. Meanwhile, there are some observables for which neither time-dependent nor static linear response yield a consistent value of T_{eff}, including the deviatoric pressure

43

and the vorticity component of the pressure [78]. Nevertheless, the effective temperature concept has proven to be robust for sheared model glass-formers, with consistent values also measured from the derivative of entropy with respect to energy [72, 81, 87] and the fluctuations of a low-frequency harmonic oscillator [27]. Most recently, Ilg and Barrat [54] showed that T_{eff} controls activated transition rates of a test probe consisting of a dimer connected by a double-well potential and embedded in a sheared model glass. The rate of crossing the energy barrier separating the two wells has an Arrhenius form $\exp(-\Delta E/T_{\text{eff}})$, where T_{eff} is consistent with previous definitions.

3.2 Effective Temperature Controls Material Properties

In this section, we shift the focus from testing the validity of the effective temperature to examining its importance for material properties. We will focus on the role of effective temperature in the jamming phase diagram parameterized by T/p, σ/p, and p in section 3.3. First, we establish the relationship between T_{eff} and material properties such as the shear stress.

In this section, we study the two-dimensional analog of the system from chapter 2, 50:50 mixtures of disks of diameter ratio 1 : 1.4 and equal mass. The disks interact via a purely repulsive harmonic potential ($\alpha = 2$). We fix the area fraction at $\phi = 0.9$. Most of the results are based on simulations of 400 disks, but we carried out simulations of up to 6400 disks to confirm that none of these results have any appreciable system size dependence. Units in this section are

measured with the smaller particle diameter, the interaction spring constant, and the particle mass set equal to 1. This yields a unit time period on the order of a binary collision time. We uniformly and steadily shear the system at a strain rate $\dot{\gamma}$ and couple the system to a heat bath at temperature T by solving the Sllod equations of motion with Lees-Edwards periodic boundary conditions and a Gaussian thermostat [4]. We integrate these equations using a fourth-order Gear corrector-predictor algorithm with a time step of 0.01. We obtain the same results with a Nosé-Hoover thermostat. We use between five and twenty simulation runs for each set of $(T, \dot{\gamma})$. For each simulation, we collect data over at least nine strain units after an equilibration period of several strain units.

We measure T_{eff} from the relation between the static linear response and the variance of the pressure [4, 81]. In equilibrium at fixed N, T, and A, this relation is

$$\frac{A}{T}\langle(\delta p)^2\rangle = A\left(\frac{\partial\langle p\rangle}{\partial A}\right)_T + \langle p\rangle + \frac{\langle x\rangle}{A}, \tag{3.3}$$

where p is the pressure, A is the area, and x is the hypervirial as defined in [4]. T_{eff} is defined by replacing T with T_{eff} in the left hand side of Eq. (3.3). We measure $\partial\langle p\rangle/\partial A$ by running simulations at $\phi = 0.897$ and $\phi = 0.903$, using the same protocol and a similar quantity of simulations as for $\phi = 0.9$. Measurements from this definition have been compared to those from many other definitions of T_{eff} for a zero-temperature sheared foam [81]. We find that T_{eff} is consistent with less precise measurements of T_{eff} defined by the Green-Kubo relation for shear viscosity [4, 81]. O'Hern et al. [78] showed that T_{eff} from pressure fluctuations agrees with that derived from the time-dependent linear response of

density fluctuations [10] over a range of parameters for the system we use. We also find consistency between these two definitions, except at very low strain rates where the logarithmic time-dependence of the diffusivity, expected in two dimensions [59], is apparent within the time scale of the density correlation function. This long-time tail does not affect the viscosity because at the high area fraction and low temperatures studied, the kinetic contribution to the viscosity is much smaller than the potential contribution.

Figure 3.1 shows the measured quantities, stress σ and effective temperature T_{eff}, as functions of bath temperature T and strain rate $\dot{\gamma}$. Figure 3.1(a) shows a bifurcation of σ about a dynamic glass transition temperature $T_0 \approx 0.0012$ at low $\dot{\gamma}$, similar to the bifurcation at fixed pressure discussed in section 2.3. The two sides of the bifurcation in Fig. 3.1(a) describe two different low-$\dot{\gamma}$ limits. On the $T > T_0$ side, σ approaches $\sigma \sim \dot{\gamma}$ at low $\dot{\gamma}$, suggesting that the shear viscosity $\eta \equiv \sigma/\dot{\gamma}$ enters a Newtonian regime for $T > T_0$ and sufficiently low $\dot{\gamma}$. For $T \geq 0.0017$, we have reached strain rates low enough that η becomes independent of $\dot{\gamma}$. We define the equilibrium viscosity η_{eq} as the shear viscosity in this Newtonian regime. For $T_0 < T < 0.0017$, we do not reach the Newtonian regime at accessible time scales/strain rates. However, we find that for all $T \geq 0.0015$, $\eta(\dot{\gamma})$ is well-described by the phenomenological Ellis equation [111], $1/\eta(\sigma) = 1/\eta_0 + m^{-1/n}\sigma^{(1-n)/n}$, which interpolates between Newtonian and power law rheology and allows us to define η_{eq} down to $T = 0.0015$. In contrast, for $T < T_0$ we observe apparent yield stress rheology on the time scale of our simulations [96]. We find $\sigma - \sigma_{\text{yield}} \propto \dot{\gamma}^b$ over the lowest two decades of $\dot{\gamma}$ that our simulation can access, with the exponent b ranging between 0.4 ($T = 0.0012$) and 0.6 ($T = 0.0001$), similar to that observed
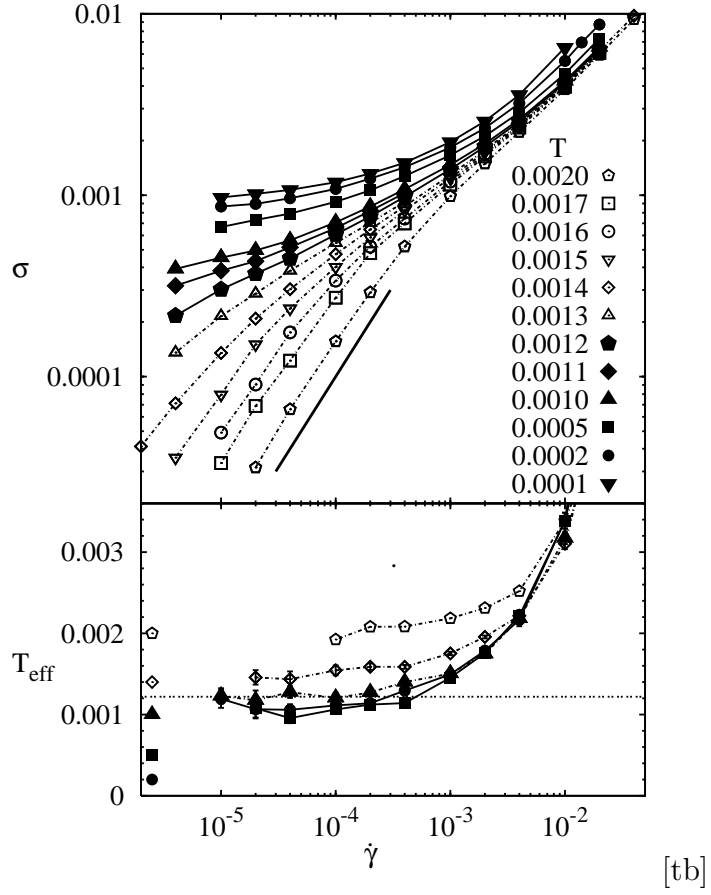
Figure 3.1: Shear stress σ (a) and effective temperature T_{eff} (b) vs shear strain rate $\dot{\gamma}$ for several values of temperature T. In all figures, dashed lines and open points indicate $T > T_0$. Solid lines and solid points indicate $T < T_0$. In (a), the straight line indicates a slope of 1, expected for a Newtonian fluid. In (b), the horizontal line indicates T_0, while the isolated points near the left axis indicate the values of T.

47

in emulsions [75]. This implies that the viscosity diverges as $\eta = \sigma/(\sigma - \sigma_{\text{yield}})^{1/b}$ as $\sigma \to \sigma_{\text{yield}}$.

Figure 3.1(b) shows the dependence of T_{eff} on T and $\dot{\gamma}$. For all T, T_{eff} approaches a limiting value in the quasistatic limit, $\dot{\gamma} \to 0$. For $T > T_0$, that limiting value is simply T. However, for $T < T_0$, T_{eff} appears to saturate to a value $T_{\text{eff},0}$ near T_0 [81]. Such a saturation of T_{eff} at low $\dot{\gamma}$ has been observed in experiments on sheared granular packings [97, 23, 103]. This apparent quasistatic limit suggests that $T_{\text{eff},0}$ is a property of the unsheared glass at bath temperature T, describing the disorder associated with different minima in the energy landscape [62].

In Fig. 3.2(a), we compare the approach to jamming as $T \to T_0$ with the approach at fixed $T < T_0$ and $\dot{\gamma} \to 0$, parameterizing the latter approach by T_{eff} rather than $\dot{\gamma}$. The dependence of η on $1/T_{\text{eff}}$ is similar to that of η_{eq} on $1/T$ [66], but we find no collapse among the different approaches to jamming. Along the equilibrium approach, η has the Arrhenius form $\eta = \eta_\infty \exp(E_A/T)$ at high T. The non-equilibrium approaches exhibit no Arrhenius regime in η. However, another reasonable measure of relaxation time, $\tau_{\text{shear}} \equiv \dot{\gamma}^{-1}$ (not shown), does vary in Arrhenius fashion with T_{eff} at high T_{eff}. Along all approaches, η is super-Arrhenius for T_{eff} near T_0 or $T_{\text{eff},0}$.

Figure 3.2(b) demonstrates that the stress σ collapses as a function of T_{eff} in the shear-dominated regime. We find that σ varies between two limits, depending on T and $\dot{\gamma}$. For $T > T_0$ and $\dot{\gamma} \to 0$, the shear stress approaches the Newtonian limit, $\sigma = \eta_{\text{eq}}\dot{\gamma}$, while T_{eff} approaches T. In this regime, thermal fluctuations T dominate over shear-induced ones. However, for $T \ll T_0$ and any $\dot{\gamma}$, or for $T \gtrsim T_0$ and high
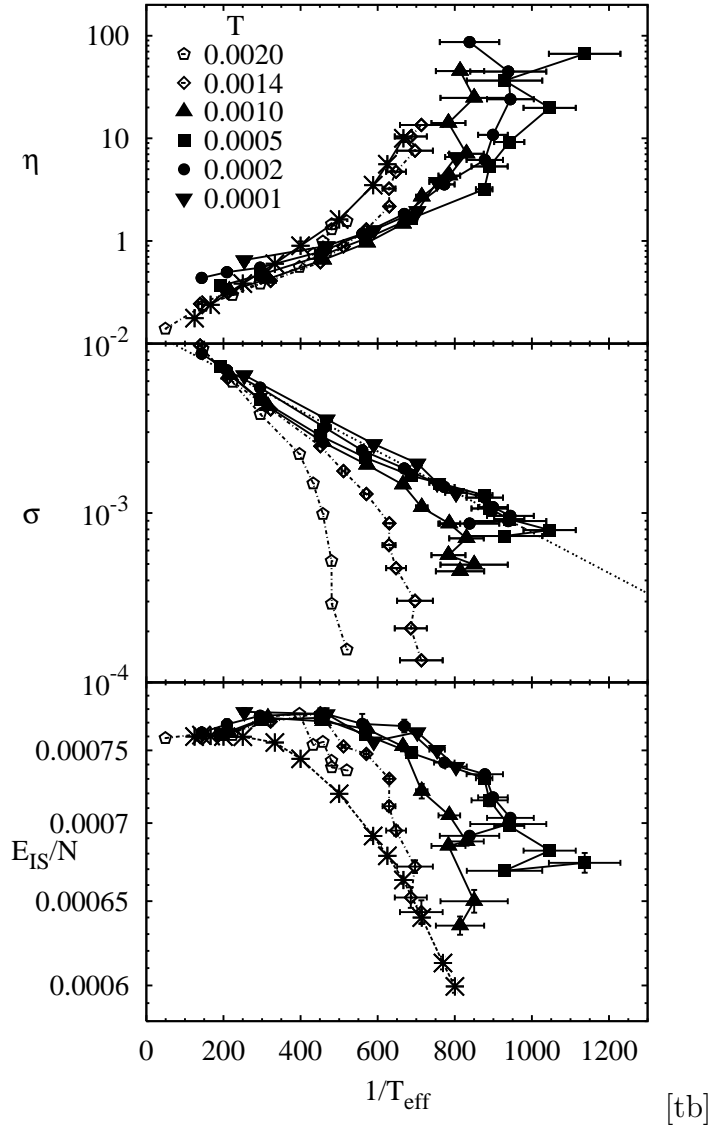
Figure 3.2: (a) Viscosity η vs $1/T_{\text{eff}}$ for several values of T and $\dot{\gamma}$. Asterisks correspond to the Newtonian viscosities ($\dot{\gamma} \to 0$, $T_{\text{eff}} = T$). (b) σ vs. $1/T_{\text{eff}}$. The straight dotted line is a fit to the form $\sigma = \sigma_0 \exp(-\Delta E/T_{\text{eff}})$ for the three lowest bath temperatures. (c) $\langle E_{\text{IS}} \rangle$ vs. $1/T_{\text{eff}}$. Asterisks indicate $\langle E_{\text{IS}} \rangle$ for $\dot{\gamma} = 0$ ($T_{\text{eff}} = T$).

$\dot{\gamma}$, the system crosses over to another regime, where shear-induced fluctuations dominate over thermal ones. In this shear-driven regime, σ depends on T and $\dot{\gamma}$ only through T_{eff}. The dependence of σ on T_{eff} follows the simple form

$$\sigma \approx \sigma_0 \exp\left(-\frac{\Delta E}{T_{\text{eff}}}\right), \tag{3.4}$$

represented by a dotted line in Fig. 3.2(b). The collapse of the data from different T and $\dot{\gamma}$ onto this same curve indicates that the dynamics are most properly described as being controlled by T_{eff}, not $\dot{\gamma}$ or T. In the shear-dominated regime, the height of the energy scale, $\Delta E = 0.0028 \pm 0.0001$, is independent of T and $\dot{\gamma}$. Its value is comparable to the activation energy $E_A = 0.0023 \pm 0.0002$ extracted from the high-T equilibrium Arrhenius relationship $\eta = \eta_\infty \exp(E_A/T)$. The correspondence between σ and T_{eff} suggests that the existence of a finite yield stress would imply a nonzero quasistatic value of $T_{\text{eff},0}$.

Equation (3.4) suggests a simple scenario. Suppose that the power per unit area supplied globally by shearing, $\sigma\dot{\gamma}$, were used to overcome local energy barriers of height ΔE at a rate of R transitions per unit area per unit time. Using $\sigma\dot{\gamma} = R\Delta E$ and the observed Eq. (3.4), we find

$$R = R_0 \dot{\gamma} \exp\left(-\frac{\Delta E}{T_{\text{eff}}}\right), \tag{3.5}$$

with $R_0 = \sigma_0/\Delta E = 4 \pm 1$. This implies that the rate of barrier crossing is Arrhenius in T_{eff} with an attempt frequency proportional to the strain rate $\dot{\gamma}$. Local rearrangements whose rate scales with $\dot{\gamma}$ are observed in foam experiments [42] and simulations [101], as well as in athermal quasistatic simulations of soft disks [73].

50

Although it was derived from a steady-state relationship, Eq. 3.5 motivates a hypothesis for the time evolution of T_{eff}. Such equations [63, 69] have been used in the context of shear transformation zone (STZ) theory [36]. Following previous work [69], we suppose that the equation should balance a heating rate proportional to the work done on the system with a relaxation rate proportional to $\exp(-E_1/T_{\mathrm{eff}})$. As in Eq. 3.5 and differing from [69], we suggest that the relaxation rate should depend on a scalar rate at which the system explores new configurations. These considerations yield

$$\dot{T}_{\mathrm{eff}} \propto Q - \nu \exp\left(-\frac{E_1}{T_{\mathrm{eff}}}\right), \tag{3.6}$$

where $Q \propto \sigma\dot{\gamma}$ [65] and the attempt frequency $\nu \propto \dot{\gamma}$ in the case of steady-state shear. Equation 3.6 is consistent with Eq. 3.4 in the steady-state limit. For T_{eff} near its steady-state value $T_{\mathrm{eff,SS}}$, Eq. 3.6 reduces to $\dot{T}_{\mathrm{eff}} \propto \sigma\dot{\gamma}(T_{\mathrm{eff,SS}} - T_{\mathrm{eff}})$, as used in STZ theory [63].

The scenario suggested by Eqs. 3.5-3.6 is that T_{eff} activates the system over barriers whose height is independent of T_{eff}. However, measurements of the average inherent structure energy $\langle E_{\mathrm{IS}}\rangle$ [98] of the system suggest that the height of energy barriers does depend on T_{eff}. We measure E_{IS} of the sheared system by taking configurations explored during steady-state shear and quenching them to their local energy minima by the conjugate-gradient technique. For comparison, we also measure $\langle E_{\mathrm{IS}}\rangle(T_{\mathrm{eff}} = T)$ for the equilibrium system at $\dot{\gamma} = 0$ above the glass transition temperature. Fig. 3.2(c) shows that $\langle E_{\mathrm{IS}}\rangle(T_{\mathrm{eff}} = T)$ is flat at high T. For $T < T_{MC}$, where T_{MC} marks the onset of super-Arrhenius be-

51

havior in Fig. 3.2(a), we find that $\langle E_{\text{IS}} \rangle (T_{\text{eff}} = T)$ decreases monotonically with decreasing T, in agreement with [56]. At low T, the system visits deeper potential energy basins, presumably separated by higher barriers, consistent with the super-Arrhenius viscosity $\eta = \eta_\infty \exp(E_A(T)/T)$, where $E_A(T)$ is the T-dependent barrier height.

Figure 3.2(c) shows that $\langle E_{\text{IS}} \rangle (T_{\text{eff}})$ of the sheared system is distinct from the equilibrium curve [62] but also decreases as $T_{\text{eff}} \to T_{\text{eff},0}$. Moreover, the data appear to collapse in the shear-dominated regime, as in Fig. 3.2(b). At sufficiently low T and/or high $\dot\gamma$, the data collapse onto a single curve, but cross over to the equilibrium curve at high T and low $\dot\gamma$. For each T, the point at which $\langle E_{\text{IS}} \rangle (T_{\text{eff}})$ begins to decrease corresponds to the upturn of viscosity, suggesting that energy barriers increase with decreasing $\langle E_{\text{IS}} \rangle$.

In summary, there are two possible explanations for the upturn of η as $T_{\text{eff}} \to T_{\text{eff},0}$. The first explanation is that relaxation rates are controlled by T_{eff}-activated transitions over barriers whose heights increase with decreasing T_{eff}. This view is supported by an STZ analysis of our data [64]. The second explanation is that the barrier heights overcome during the shearing process do not depend strongly on T_{eff}, even though the energy minima decrease with decreasing T_{eff}. In that case, the super-Arrhenius behavior is due to Eq. 3.4 and the divergence in $\eta \approx \sigma_{\text{yield}}/\dot\gamma$ as $\dot\gamma \to 0$. Further study, particularly of transients, is needed to resolve this issue.

Finally, we revisit the issue of the validity of the effective temperature concept. Nine independent definitions of temperature have been shown to yield consistent values of T_{eff}, within numerical error: the relation of density [10, 78] and pressure fluctuations [78] at nonzero wavevectors to the associated response at long times;

52

the relation of fluctuations in the total pressure, stress, and energy to static response [78, 81]; the Einstein relation between diffusion and drag [10, 72, 81]; the derivative of entropy with respect to energy [72, 81]; the fluctuations of a low-frequency harmonic oscillator [27]; and the barrier crossing rate of a test two-level system [54]. However, there are definitions that do not yield consistent values of T_{eff}: the relation of fluctuations in the total deviatoric pressure and in the vorticity component of pressure to the response at long times [78]. Thus, the concept of effective temperature, even when restricted to long-time-scale properties, is only approximate [24, 92].

If the concept of effective temperature is not rigorously valid for sheared glasses, why would it be of any interest for these systems? Our results provide an answer: the effective temperature critically affects materials properties by setting the energy scale for fluctuations that kick flowing glasses over energy barriers.

3.3 Effective Temperature in the Hard-Sphere Limit

In order to understand how the effective temperature relates to the dimensionless jamming phase diagram we established in chapter 2, in this section we measure the effective temperature for sheared hard spheres. We find that there is a consistent value of effective temperature T_{eff} for different measurements. Moreover, we find that in order for the hard sphere system to flow on accessible time scales, the ratio of the effective temperature to the pressure must exceed a threshold value, regardless of whether the system is fluidized primarily by temperature or

53

by shear. This suggests that the dynamic glass transition in the plane spanned by the dimensionless temperature and the dimensionless shear stress is controlled by the same mechanism, the competition between low-frequency fluctuations and the confining pressure. We also investigate the effective temperature at shear stresses well above threshold. We find that the relaxation time decreases as a function of increasing effective temperature in roughly the same manner as in equilibrium. We find that within a shear-dominated regime, the shear stress collapses as a function of the effective temperature, following a roughly exponential form with an activation energy proportional to the pressure. Following the results of chapter 2, we expect our results to hold for soft spheres in the universal limit $p \to 0$, and we expect that the behavior of the effective temperature at higher pressures may be understood in terms of corrections of order p.

We consider the same hard sphere model as in chapter 2, a collection of frictionless hard spheres of mass m, half with diameter d and half with diameter $1.4d$. We calculate the shear stress, the pressure, and the effective temperature by conducting event-driven molecular dynamics simulations [55, 74] at fixed kinetic temperature T, packing fraction ϕ, and shear strain rate $\dot{\gamma}$. We define the kinetic temperature by the velocity fluctuations relative to a uniform shear gradient imposed by Lees-Edwards boundary conditions. We periodically rescale the velocities in order to keep the temperature within 1% of the desired value. Since there is no energy scale in the model, the kinetic temperature serves only to set the time scale for thermal fluctuations, so we may set $T = 1$ without loss of generality. Results in this section are presented in units such that $T = m = d = 1$.

We find that two definitions of effective temperature yield consistent results:

the compressibility temperature T_χ relating the measured isothermal compressibility with that expected from the zero-wavevector limit of the structure factor [44, 82], and the viscosity temperature T_η relating the measured shear viscosity with that expected from the Einstein-Helfand expression [3, 39, 50]. The pressure temperature T_p relating the measured pressure with that expected from the radial distribution function at contact [44] yields a value consistent with the kinetic temperature T.

In chapter 2 we showed that the behavior of hard spheres, as well as soft spheres at sufficiently low pressure, is controlled by the dimensionless numbers T/pd^3 and σ/p. In order for the spheres to flow on accessible time scales, the dimensionless temperature T/pd^3 and the dimensionless shear stress σ/p must fall within the fluid portion of the diagram at large T/pd^3 and/or large σ/p. In the absence of shear, the dimensionless temperature must exceed a glass transition value of $T/pd^3 \approx 0.08$. At lower dimensionless temperatures, the spheres can only flow if the dimensionless shear stress σ/p exceeds a dynamic yield stress which increases smoothly from zero as T/pd^3 falls below the dynamic glass transition. Since pressure controls both the dynamic glass transition temperature and the dynamic yield stress for hard spheres, we expect that pressure will also set the scale for the effective temperature. We will therefore present results for the temperatures T_p, T_χ, and T_η in relation to the pressure.

We now state the definitions and outline the derivations of the temperatures T_p, T_χ, and T_η. The pressure temperature T_p follows from the equilibrium expression [44] relating the pressure and the radial distribution function $g(r)$ for homogeneous, isotropic fluids with only pairwise radially symmetric potentials $V(r)$. For

monodisperse hard spheres, using the fact that $y(r) = g(r) \exp(V(r)/T)$ is continuous even at the hard sphere diameter $r = d$, the expression for the pressure can be written in terms of the radial distribution function at contact [44],

$$\frac{p}{\rho T} = 1 - \frac{2}{3}\pi\rho d^3 g(d),$$ (3.7)

where $\rho = N/V$ is the number density. For mixtures of hard spheres, such as our mixture of spheres of diameter d and $1.4d$, the extression becomes

$$\frac{p}{\rho T} = 1 - \frac{2}{3}\pi\rho \sum_{\alpha,\beta} c_\alpha c_\beta d^3_{\alpha\beta} g_{\alpha\beta}(d_{\alpha\beta}),$$ (3.8)

where $V_{\alpha\beta}(r)$ is the pair potential between spheres of species α and β, $g_{\alpha\beta}(\vec{r})$ is the partial pair distribution function (normalized to equal 1 at long distances), $c_\alpha = N_\alpha/N$ is the fraction of particles of type α, and $d_{\alpha\beta} = (d_\alpha - d_\beta)/2$ is the separation at contact between species of type α and β. We therefore define the pressure temperature as

$$T_p = \frac{p}{\rho}\left(1 - \frac{2}{3}\pi\rho \sum_{\alpha,\beta} c_\alpha c_\beta d^3_{\alpha\beta} g_{\alpha\beta}(d_{\alpha\beta})\right)^{-1}.$$ (3.9)

The compressibility temperature T_χ follows from the equilibrium compressibility equation relating the $k \to 0$ limit of the structure factor $S_{ij}(k)$ and the isothermal compressibility χ_T for homogeneous, isotropic fluids. For single-component fluids the compressibility equation is [44, 82]

$$\rho T \chi_T = S(0).$$ (3.10)

56

For multiple-component fluids, the compressibility equation is

$$\rho^2 T \chi_T = |B| / \sum_{\alpha,\beta} c_\alpha c_\beta |B|_{\alpha\beta}, \qquad (3.11)$$

where $B_{\alpha\beta} = c_\alpha \delta_{\alpha\beta} + c_\alpha c_\beta G_{\alpha\beta}$, $G_{\alpha\beta} = \int d\vec{r}(g_{\alpha\beta}(\vec{r}) - 1)$, and $|B|_{\alpha\beta}$ denotes the cofactor of $B_{\alpha\beta}$ in the determinant $|B|$ [60]. Since $G_{\alpha\beta}$ are related to the zero-wavevector values of the partial structure factors $S_{\alpha\beta}(0)$ via $S_{\alpha\beta}(0) = \delta_{\alpha\beta} + \rho\sqrt{c_\alpha c_\beta} G_{\alpha\beta}$ for a homogeneous, isotropic fluid, we can rewrite the compressibility equation in terms of the partial structure factors. We define the partial structure factors as in [7] by

$$S_{\alpha\beta}(\vec{k}) = (N_\alpha N_\beta)^{-1/2} \left\langle \sum_{i,j} \exp(i\vec{k} \cdot (\vec{r}_{\alpha,i} - \vec{r}_{\beta,j})) \right\rangle - (N_\alpha N_\beta)^{1/2} \delta_{k,0}, \qquad (3.12)$$

where the positions $\vec{r}_{\alpha,i}$ are indexed by their species α and the multiplicity of each species $i = 1, ..., N_\alpha$. For a two-component mixture, the compressibility equation becomes [7]

$$\rho T \chi_T = \frac{S_{11}(0)S_{22}(0) - (S_{12}(0))^2}{x_1 S_{22}(0) + x_2 S_{11}(0) - 2\sqrt{x_1 x_2} S_{12}(0)}. \qquad (3.13)$$

We therefore define the compressibility temperature as

$$T_\chi = \frac{1}{\rho \chi_T} \frac{S_{11}(0)S_{22}(0) - (S_{12}(0))^2}{x_1 S_{22}(0) + x_2 S_{11}(0) - 2\sqrt{x_1 x_2} S_{12}(0)}. \qquad (3.14)$$

While the isothermal compressibility χ_T is unambiguously defined in equilibrium, when measuring χ_T out of equilibrium, we must choose how to fix the nonequilibrium driving force. Since the dimensionless shear stress σ/p plays a similar role as the dimensionless temperature T/p, we choose to fix the dimensionless shear

stress σ/p. This choice makes a difference of up to order 10% relative to fixing the shear strain rate $\dot{\gamma}/\sqrt{T}$ or the dimensionless shear strain rate $\dot{\gamma}/\sqrt{p}$ and improves the agreement with the T_η.

The shear viscosity temperature follows from the equilibrium Einstein-Helfand expression

$$T\eta = \lim_{t\to\infty} \frac{dH(t)}{dt}, \tag{3.15}$$

where $H(t) = (1/2VT)\langle|G_\eta(t) - G_\eta(0)|^2\rangle$, $G_\eta = \sum_i m_i \dot{x}_i y_i$, and η is the shear viscosity [3, 39, 50]. We define T_η as the slope of $H(t)/\eta$ vs t at long times. Since $\langle G_\eta \rangle$ does not vanish under shear, we must amend amend the definition of H to be

$$H(t) = \frac{1}{2VT} \left\langle |G_\eta(t) - G_\eta(0) - \sigma V t|^2 \right\rangle, \tag{3.16}$$

similar to how the equilibrium bulk viscosity is treated under the Einstein-Helfand formulation [39]. We therefore define the shear viscosity temperature as the long-time limit of

$$T_\eta = \frac{1}{\eta} \frac{dH(t)}{dt}. \tag{3.17}$$

While the shear viscosity η is unambiguously defined in equilibrium, out of equilibrium, due to the shear thinning effect, we must choose between the differential viscosity $d\sigma/d\dot{\gamma}$ and the linear viscosity $\sigma/\dot{\gamma}$. Following the definition of effective temperature for shear stress fluctuations that yields a consistent value for soft spheres [81], we define the viscosity η as the linear viscosity. This choice makes a difference of up to a factor of 2. Choosing the differential viscosity yields a temperature that is inconsistent with the compressibility temperature in the
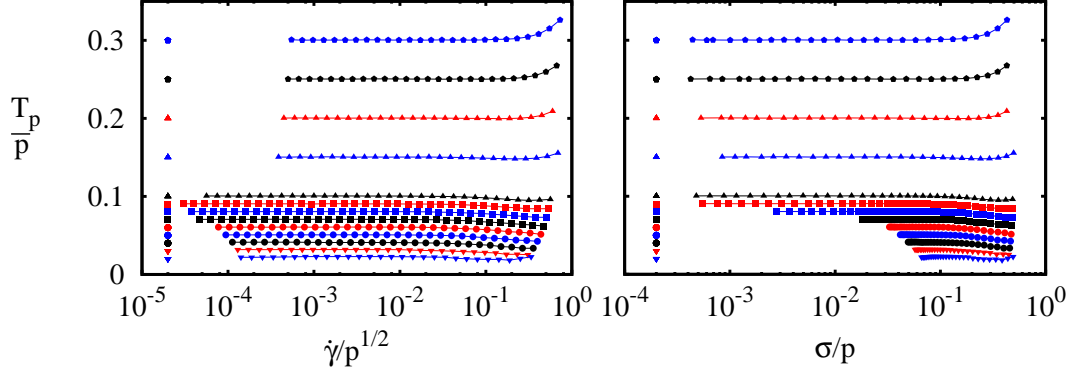
Figure 3.3: Dimensionless pressure temperature T_p/p vs (a) dimensionless strain rate $\dot{\gamma}/\sqrt{p}$ and (b) dimensionless shear stress σ/p. Each connected curve represents a different dimensionless temperature T/p indicated by the symbols on the right side of the plot. The values are (top to bottom): $T/p = 0.3$ (blue hexagons), 0.25 (black hexagons), 0.2 (red up triangles), 0.15 (blue up triangles), 0.1 (black up triangles), 0.09 (red squares), 0.08 (blue squares), 0.07 (black squares), 0.06 (red circles), 0.05 (blue circles), 0.04 (black circles), 0.03 (red down triangles), and 0.02 (blue down triangles).

shear-thinning regime.

We now show the results for the temperatures T_p, T_χ, and T_η. Following our experience with soft spheres, we expect that the temperatures fall into two classes, one agreeing with the environment temperature T and the other describing an effective temperature. Throughout this section, we restrict our results to $\sigma/p <$ 0.5, the range over which we observe no layering, as discussed in section 2.3.

Figure 3.3 shows the dimensionless pressure temperature T_p/p vs (a) the dimensionless strain rate $\dot{\gamma}/\sqrt{p}$ and (b) the dimensionless pressure σ/p. We interpolate our fixed-packing-fraction data to create curves of equal dimensionless temperature T/p. For all temperatures, the pressure temperature equals the kinetic temperature and is insensitive to shearing. This result is expected considering
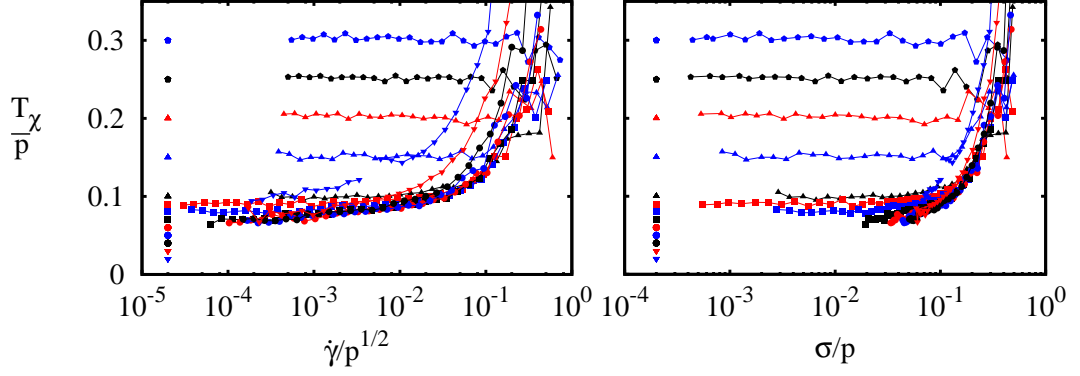
Figure 3.4: Dimensionless compressibility temperature T_χ/p vs (a) dimensionless strain rate $\dot{\gamma}/\sqrt{p}$ and (b) dimensionless shear stress σ/p. Each connected curve represents a different dimensionless temperature T/p indicated by the symbols on the right side of the plot. The values are (top to bottom): $T/p = 0.3$ (blue hexagons), 0.25 (black hexagons), 0.2 (red up triangles), 0.15 (blue up triangles), 0.1 (black up triangles), 0.09 (red squares), 0.08 (blue squares), 0.07 (black squares), 0.06 (red circles), 0.05 (blue circles), 0.04 (black circles), 0.03 (red down triangles), and 0.02 (blue down triangles).

that the pressure is dominated by high-frequency fluctuations characterized by T.

Figure 3.3 shows the dimensionless compressibility temperature T_χ/p vs (a) the dimensionless strain rate $\dot{\gamma}/\sqrt{p}$ and (b) the dimensionless pressure σ/p. The results are reminiscent of the effective temperature for soft spheres discussed in section 3.2 [48]. At high temperatures and low strain rates, the compressibility temperature agrees with the kinetic temperature T. However, for temperatures below the dynamic glass transition temperature $T_g/p \approx 0.08$, the compressibility departs strongly from the kinetic temperature, even at low strain rates. The dynamic glass transition temperature appears to control the compressibility temperature at low temperatures and strain rates: on the time strain rates accessible to our simulations, the compressibility temperature always stays at or above the
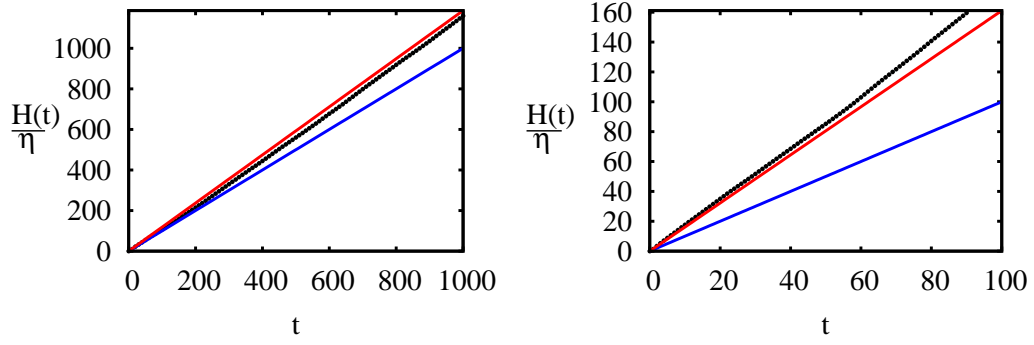
Figure 3.5: $H(t)/\eta$ vs t for packing fraction $\phi = 0.58$ and two characteristic shear strain rates (a) $\dot{\gamma}/\sqrt{p} = 2.65 \times 10^{-3}$ and (b) $\dot{\gamma}/\sqrt{p} = 2.44 \times 10^{-2}$. The black curves are $H(t)/\eta$, whose derivative at long times equals T in equilibrium. For comparison, the blue lines represent the function Tt, and the red curves represent the function $T_\chi t$. The three state points correspond to dimensionless temperature and dimensionless stress of $T/p = 7.52 \times 10^{-2}$ and $\sigma/p = 1.46 \times 10^{-2}$; $T/p = 7.00 \times 10^{-2}$ and $\sigma/p = 5.01 \times 10^{-2}$; and $T/p = 5.95 \times 10^{-2}$ and $\sigma/p = 1.19 \times 10^{-1}$; respectively.

dynamic glass transition value, $T_\chi/p \geq T_g/p \approx 0.08$. Notice that most of the data at low kinetic temperature collapse onto a narrow band of compressibility temperatures, except for the very lowest kinetic temperature, $T/p = 0.02$ (blue down triangles), for which the compressibility temperature is significantly higher.

In order for the compressibility temperature to be a useful effective temperature, it must at least agree with an independent measurement of temperature. For comparison, we measure the viscosity temperature T_η defined by Eq. 3.17. In order to measure T_η, we must access the long-time asymptotic regime of $dH(t)/dt$ in Eq. 3.17, which we find occurs for t on the order of 10τ, where τ is relaxation time. We calculate $H(t)$ by averaging over a long trajectory with overlapping intervals of length t. In equilibrium, we find that we can only reliably reproduce the equilibrium Einstein-Helfand expression if we average over a trajectory of length

61

$100t$ or more. We must therefore simulate trajectories of at least 1000τ in order to calculate T_η. Considering this computational expense, we do not measure T_η for the entire parameter space represented in Fig. 3.4; rather, we check that the derivative of $dH(t)/dt$ agrees with the compressibility temperature T_χ for several representative sets of parameters. Fig. 3.5 shows two typical examples near the dynamic glass transition, one at a low shear strain rate and one at a higher shear strain rate. In both cases, as well as for the other cases examined, we find that the derivative of $H(t)/\eta$, represented by black circles in Fig. 3.5, is closer to T_χ, represented by a solid red line, than by T, represented by a solid blue line. This indicates that the Einstein-Helfand expression, Eq. 3.16, holds with T replaced by T_χ. In other words, both the compressibility temperature T_χ and the viscosity temperature T_η yield consistent values, even in the region of parameter space where they disagree with the kinetic temperature T. We therefore consider $T_{\mathrm{eff}} = T_\chi = T_\eta$ to be the effective temperature of the hard sphere fluid.

We now investigate how the effective temperature controls the material properties of the hard sphere fluid. In Fig. 3.6 we show Arrhenius-type log-linear plots of (a) the dimensionless relaxation time $\tau\sqrt{p}$ and (b) the dimensionless shear stress σ/p vs the inverse dimensionless effective temperature p/T_χ. As in chapter 2, we define the relaxation time as the time at which the root mean square displacement equals 1.

Figure 3.6 (a) shows the dimensionless relaxation time $\tau\sqrt{p}$ vs inverse dimensionless effective temperature p/T_χ. Each curve represents a different value of the dimensionless kinetic temperature T/p over a range of strain rates. Except for $T/p \leq 0.03$ well below the dynamic glass transition $T_g/p \approx 0.08$, the curves
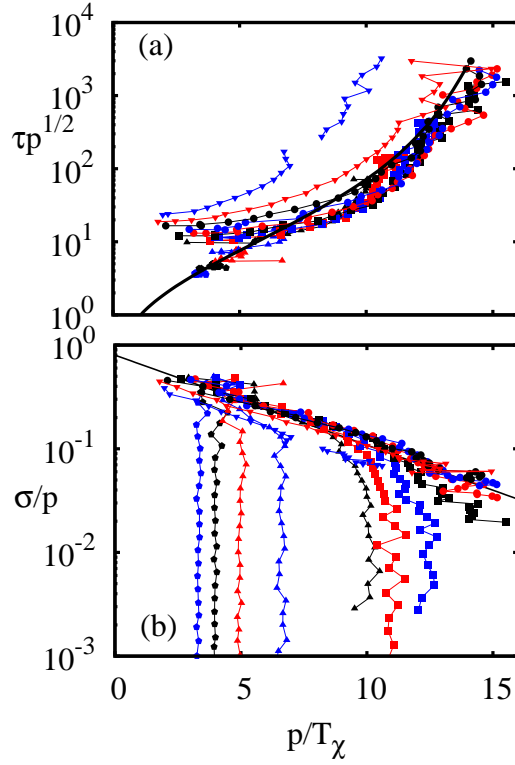
Figure 3.6: Log-linear plots of (a) dimensionless relaxation time $\tau\sqrt{p}$ and (b) dimensionless shear stress σ/p vs inverse dimensionless effective temperature p/T_χ. Each connected curve represents a different dimensionless temperature T/p indicated by the symbols on the right side of the plot. The values are (top to bottom): $T/p = 0.3$ (blue hexagons), 0.25 (black hexagons), 0.2 (red up triangles), 0.15 (blue up triangles), 0.1 (black up triangles), 0.09 (red squares), 0.08 (blue squares), 0.07 (black squares), 0.06 (red circles), 0.05 (blue circles), 0.04 (black circles), 0.03 (red down triangles), and 0.02 (blue down triangles). In (a), the black curve represents the equilibrium data under no shear. For the equilibrium data, we use the kinetic temperature T instead of the compressibility temperature T_χ as the effective temperature. In (b), the straight line is a guide to the eye following the equation $\sigma/p = 0.8\exp(0.2T_\chi/p)$.

63

for various kinetic temperatures fall mostly onto a narrow band of values. This indicates that the relaxation time depends mostly on the effective temperature T_χ, which in general is not equal to the environment temperature T, and not separately on the environment temperature T. Moreover, except at very high effective temperatures, $p/T_\chi < 5$, this band of values closely coincides with the equilibrium curve. To construct the equilibrium curve, we use the kinetic temperature T rather than the compressibility temperature T_χ because the signal is better, but we obtain similar results using the compressibility temperature, because $T_\chi = T$ in equilibrium. Note by comparing to Fig. 3.6 (b) that high effective temperatures $p/T_\chi < 5$ correspond generally to high shear stresses $\sigma/p > 0.3$. At such high shear stresses, where the interactions are highly anisotropic, we do not expect that the mechanisms for relaxation should agree with the mechanisms in equilibrium.

In figure 3.6 (b) we show the dimensionless shear stress σ/p vs the inverse dimensionless effective temperature p/T_χ. We find results qualitatively similar to those of Fig. 3.2 (b) in section 3.2 [48], due to the fact that the pressure does not vary greatly with temperature or strain rate for the soft sphere system at the packing fraction well above close packing used in section 3.2. However, now we have a better understanding for the universal character of the functional relationship between σ/p and p/T_χ. As in section 3.2, we find that parameter space can be divided into two regimes, a temperature-dominated regime and a shear-dominated regime. In the temperature-dominated regime, the effective temperature coincides with the kinetic temperature over a range of applied shear stress. Data within this regime fall along vertical connected curves in Fig. 3.6 (b). We find that this regime

64

also coincides with where $\tau\sqrt{p}$ is insensitive to σ/p and the shear strain rate is proportional to the shear stress by a Newtonian shear viscosity. The first effect is apparent in Fig. 3.6 (a), where the data within the temperature-dominated regime appear as groups of points clustered within a small range of p/T_χ and $\tau\sqrt{p}$.

At high shear stress, the data cross over to a shear-dominated regime, where the dimensionless shear stress σ/p depends roughly exponentially on the inverse dimensionless effective temperature p/T_χ and does not separately depend on the kinetic temperature. As discussed in section 3.2, the form of this dependence,

$$\frac{\sigma}{p} \approx 0.8 \exp\left(-\frac{0.2p}{T_\chi}\right), \tag{3.18}$$

suggests a simple scenario. Balancing the power per unit volume supplied by shearing, $\sigma\dot{\gamma}$, with the rate R of transitions costing energy ΔE, Eq. 3.18 implies that the transition rate is given by

$$R = R_0\dot{\gamma} \exp\left(-\frac{\Delta E}{T_\chi}\right), \tag{3.19}$$

where the energy cost ΔE is proportional to the pressure via $\Delta E \approx 0.2pd^3$ and $R_0 \approx 4$. Observing this relationship for hard spheres allows us to make a geometric interpretation of the rate of rearrangements that relax the stress. Eq. 3.19 implies that rearrangements are Arrhenius in the effective temperature with an attempt frequency proportional to the strain rate and an activation energy equal to the amount of work necessary to open up an amount of free volume ν against the pressure, where $\nu \approx 0.2d^3$.

In this section, we have shown that the low-frequency fluctuations of hard

spheres under shear are characterized by an effective temperature consistently defined either by the compressibility temperature T_χ or the viscosity temperature T_η. At temperatures above the dynamic glass transition and low shear stresses, the effective temperature agrees with the kinetic temperature. Below the dynamic glass transition, the dimensionless effective temperature must exceed a threshold value equal to the dimensionless glass transition temperature, indicating that the mechanism for fluidization is similar along the dynamic glass transition curve in the $T/p - \sigma/p$ plane. Over a wide range of parameter space, the dimensionless relaxation time depends mostly on the dimensionless effective temperature and not on whether these low-frequency fluctuations are primarily due to temperature or shear. This indicates that similarities in the mechanism of relaxation persist well into the fluid portion of the jamming phase diagram. However, within this regime but at sufficiently high shear stress, a crossover is apparent in the behavior of the average shear stress. Our results suggest that at sufficiently high shear stress, the power put into the system appears to be limited by the rate R at which plastic rearrangements release energy ΔE, where ΔE is proportional to the work necessary to open up a typical void and the rate R is Arrhenius in the effective temperature.

Chapter 4

Kinetic Heterogeneities at Dynamical Crossovers

Having established the important role of fluctuations in fluidizing glass-forming liquids throughout the jamming phase diagram, we now turn to developing a microscopic understanding of these fluctuations. We focus on the temperature-mediated dynamic glass transition, but following the results of section 2.3 and chapter 3, we expect similar results under shear.

While fluctuations of static properties remain small as a fluid approaches its dynamic glass transition, the dynamics become increasingly correlated in space and heterogeneous in time. These correlations are most pronounced at time scales on the order of the relaxation time of the system and are typically quantified using a dynamic susceptibility that measures fluctuations in the number of mobile particles [5, 14, 15, 16, 26, 40, 88]. A particle is deemed mobile if it has moved a distance of at least a in a time interval t, so the dynamic susceptibility depends on

the choice of a and t. For a fixed at a fraction of the particle diameter, the dynamic susceptibility exhibits a maximum at times t on the order of the relaxation time. This maximum increases in height as temperature is lowered towards the glass transition and the relaxation time increases [15, 19, 20, 37, 41, 51, 61, 67, 77, 76, 99, 102]. Thus, the peak in the dynamic susceptibility is viewed as an important signature of the glass transition.

In molecular dynamics simulations of glass-forming liquids, the dynamic susceptibility is typically measured as a function of t with the length scale a fixed. Studies of the length-scale dependence have been more rare [1, 19, 20, 67]. However, recent experiments on granular systems [68] suggest that it is instructive to study the dynamic susceptibility as a function of a as well as t. This approach has the advantage of avoiding any arbitrariness in the choice of a or t.

In this chapter, we use the dynamic susceptibility to measure the spatial extent of kinetic heterogeneities as a function of distance a and time t [47]. At temperatures where there is a well-defined sub-diffusive plateau in the root mean square displacement, we find that there are *two* distinct local maxima in the dynamic susceptibility $\chi_{\mathrm{ss}}(a, t)$ quantifying the spatial extent of kinetic heterogeneities. These two maxima correspond to crossovers in the dynamics. The larger of the two maxima, which has been observed in previous simulations, occurs at late times at the crossover from sub-diffusive to diffusive motion. This maximum quantifies the strong and well-studied correlations in the dynamics that arise at the scale of the relaxation time. In addition, we find a secondary maximum at much earlier times, corresponding to the crossover from ballistic to sub-diffusive motion. The presence of this second maximum indicates that the dynamics also exhibit signifi-

cant spatial correlations at time scales corresponding to the trapping of a particle in the cage of its neighbors. The discovery of a second maximum implies that kinetic heterogeneities are not just associated with the onset of slow dynamics near a glass or jamming transition, and that they should be regarded more generally as symptoms of crossovers in the dynamics.

Our model consists of a two-dimensional 50:50 mixture of disks of diameters d and $1.4d$ and equal mass m. The disks interact via a purely repulsive harmonic potential ($\alpha = 2$). We choose units such that d, the interaction energy scale ϵ, and m are set equal to 1. This sets the time unit $d\sqrt{m/\epsilon} = 1$. To solve the dynamics, we perform molecular dynamics simulations at fixed temperature and pressure in square periodic cells containing $N = 100$, 400, or 1600 disks. We employ Gaussian constraints [33] to fix the instantaneous temperature $T = |\vec{p}_i|^2/2(N-1)$ and hydrostatic pressure $p = (\vec{r}_i \cdot \vec{F}_i/2 + NT)/L^2$, where $\vec{F}_i = -\vec{\nabla}\sum_j V(r_{ij})$, allowing the side length L of the periodic cell to vary. In our runs, we fix $p = 10^{-2}$ and measure the dynamics at various temperatures $T = 0.01p$ to $T = 0.09p$ by running 10 to 20 simulations for durations between $\Delta\tau = 10^5$ and $\Delta\tau = 10^7$ after equilibrating at the temperature for one fifth as long. We arrive at the temperature by quenching at rates 10^{-9} or 10^{-8} starting from well-equilibrated configurations at $T = 0.1p$. Results here are shown for a quench rate of 10^{-9}.

Correlations in the dynamics are measured by using the standard time- and distance-dependent order parameter

$$q_{\mathrm{s}}(a,t;i,\tau) \equiv w_a(\vec{r}_i(\tau) - \vec{r}_i(\tau+t)), \tag{4.1}$$

where $w_a(\vec{r})$ is an overlap function [41]. Here, $w_a(\vec{r}) = 1$ if $|\vec{r}| < a$ and 0 otherwise. We denote the average over all particles i by $Q_s(a, t; \tau) \equiv (1/N) \sum_i q_s(a, t; i, \tau)$ and its time average by $\bar{Q}_s(a, t) \equiv \langle Q_s(a, t; \tau) \rangle_\tau$. At very short times, $\bar{Q}_s(a, t) = 1$ because no particles have moved a distance a. At very long times, positions at time $\tau + t$ are uncorrelated with positions at time τ, so $\lim_{t \to \infty} \bar{Q}_s(a, t) \simeq \phi a^2/N$, where ϕ is the packing fraction. Between these two extremes, $\bar{Q}_s(a, t)$ decays smoothly from 1 to $\phi a^2/N$.

The spatial extent of fluctuations can be characterized by the variance of the overlap function over different starting times [41]

$$\chi_{ss}(a, t) \equiv N \left(\langle Q_s(a, t; \tau)^2 \rangle_\tau - \bar{Q}_s(a, t)^2 \right). \tag{4.2}$$

As shown by the counting argument of Ref. [1], $\chi_{ss}(a, t)$ is roughly the number of particles that move a distance a over a time t in a correlated manner.

Note that the spatially averaged overlap function $Q_s(a, t; \tau)$ is the self part of the order parameter $Q(a, t; \tau) \equiv (1/N) \sum_{ij} w_a(\vec{r}_i(\tau) - \vec{r}_j(\tau + t))$, and $\chi_{ss}(a, t)$ is the self-self part of the dynamic susceptibility $\chi_4(a, t) \equiv N(\langle Q(a, t; \tau)^2 \rangle_\tau - (\langle Q(a, t; \tau) \rangle_\tau)^2)$. Glotzer et al showed that the self-self part of the dynamic susceptibility dominates over the distinct-distinct and the self-distinct parts for a model glass-forming liquid [41, 67].

The color plots of Fig. 4.1 display the spatial and temporal dependence of the dynamic susceptibility $\chi_{ss}(a, t)$. The three plots represent three temperatures: one well above the dynamic glass transition $T_g \approx 0.05p$, one slightly above it, and one below T_g. In each plot, we also display the root-mean-square (rms) displacement,
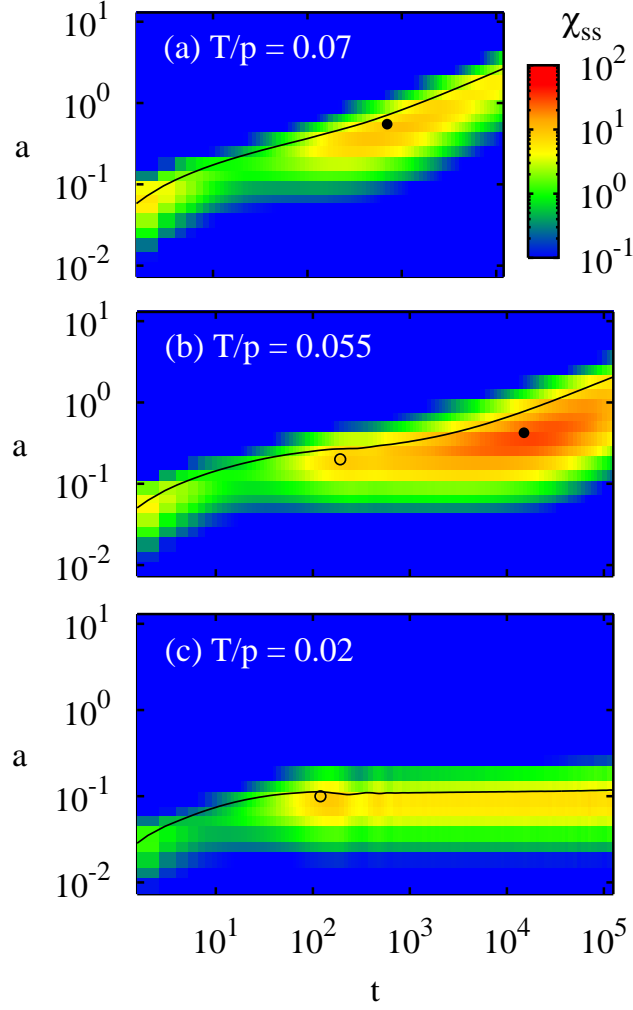
Figure 4.1: Color plots of the value of the dynamic susceptibility $\chi_{\mathrm{ss}}(a,t)$ as a function of the lag time, t, and the overlap distance, a. Results are shown at a fixed pressure, $p = 10^{-2}$, and system size, $N = 1600$, at three different temperatures: (a) $T = 0.07p$, (b) $T = 0.055p$, and (c) $T = 0.02p$. The dynamical glass transition is at $T \approx 0.05p$. For comparison, we plot the root-mean-square displacement $\Delta r(t)$ (solid curves). The circles mark the locations, $(a^\star, t^\star)$, of observed local maxima of $\chi_{\mathrm{ss}}(a,t)$. Filled circles represent cage-escaping local maxima near the end of the sub-diffusive plateau of $\Delta r(t)$. Such maxima are observed for $T \geq 0.05p$. Open circles represent cage-exploring local maxima near the beginning of the plateau. Such maxima are observed for $T \leq 0.055p$, so that there is a range of temperatures over which both local maxima exist.

$\Delta r(t) \equiv \sqrt{\langle |\vec{r}_i(0) - \vec{r}_i(t)|^2 \rangle}$. Not surprisingly, for a given t we find that $\chi_{\mathrm{ss}}(a, t)$ is largest for a near $\Delta r(t)$, the characteristic distance over which some, but not all, particles have moved. This is consistent with granular experiments by Lechenault, et al [68]. We place circles on the locations $(t^\star, a^\star)$ of the local maxima of $\chi_{ss}(a, t)$.

For the highest temperature (Fig. 4.1(a)), well above the glass transition, the rms displacement $\Delta r(t)$ shows a ballistic regime at small t, the hint of a sub-diffusive regime at intermediate times, and a diffusive regime at long times. We observe one local maximum of $\chi_{\mathrm{ss}}(a, t)$, marked by a solid circle, at the onset of the diffusive regime: the heterogeneities are largest when some particles have begun to diffuse but others remain caged. Note also that the maximum at (t^*, a^*) lies somewhat below the $\Delta r(t)$ curve, indicating that larger clusters of dynamically correlated particles are formed by less mobile particles [1].

For the intermediate temperature (Fig. 4.1(b)), the sub-diffusive plateau of $\Delta r(t)$ is well established and spreads out over two decades. Again, we observe a local maximum of $\chi_{\mathrm{ss}}(a, t)$ near the onset of the diffusive regime. However, in addition to this "cage-escaping" maximum we also observe a secondary "cage-exploring" maximum, marked by an open circle, near the onset of the plateau; the dynamics are also heterogeneous on time scales when particles are becoming constrained by their neighbors. Thus, in the regime where there are two distinct crossovers in the dynamics–one from ballistic to sub-diffusive motion, and one from sub-diffusive to diffusive motion–there are also two maxima in $\chi_{\mathrm{ss}}(a, t)$, located at

---

[1]In all cases, we also find that $\chi_{\mathrm{ss}}(a, t)$ increases along $\Delta r(t)$ with decreasing t for the shortest times observed, well within the ballistic regime, reflecting correlations in the velocities. We observe this behavior at all temperatures. This is an artifact of the barostat used; we do not observe this increase when the system is held at fixed area.

distances a and times t corresponding to the two crossovers.

For the lowest temperature shown (Fig. 4.1(c)), we do not reach a diffusive regime on the time scale of our simulation, which means that this temperature lies below the dynamic glass transition temperature $T_g \approx 0.05p$. We therefore do not observe the cage-escaping maximum associated with the onset of the diffusive regime. However, the location of the cage-exploring maximum remains relatively unchanged, as shown by the open circle. Although the system is out of equilibrium for all $T < T_g$, we observe mild aging effects only for the highest of these temperatures studied, $T = 0.04p$ and $T = 0.045p$, where the equilibration times are comparable to the quench times, waiting times, and run times of our simulations.

To study the evolution of the maxima with temperature, in Fig. 4.2 we plot $\chi_{\mathrm{ss}}(a, t)$ as a function of t for many different fixed values of a covering the same range of a as in Fig. 4.1. The thick curve marks the maximum of χ_{ss} with respect to a at each t. Maxima of this curve (marked with circles) therefore represent maxima of χ_{ss} with respect to both a and t. Fig. 4.2 shows that at high temperatures, only one local maximum of χ_{ss} can be resolved. As T is lowered, however, a shoulder becomes apparent at time scales corresponding to cage exploring. This shoulder evolves into a maximum as T is lowered still further and the higher cage-escaping maximum moves to later times. Thus, the reason why we only see two maxima at temperatures fairly close to the glass transition is because the smaller cage-exploring maximum is obscured by the higher cage-escaping maximum at higher temperatures.

The two local maxima of χ_{ss} depend very differently on temperature. In Fig. 4.3, we plot the amplitude of the maxima $\chi^\star$ and their associated locations in
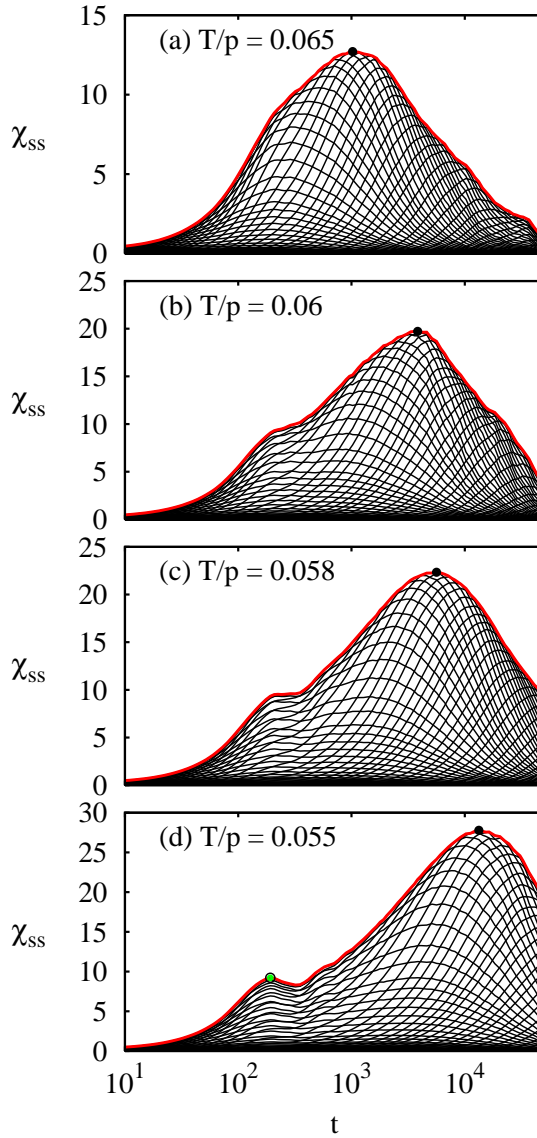
Figure 4.2: Dynamic susceptibility $\chi_{\mathrm{ss}}(a, t)$ vs lag time t for $p = 10^{-2}$, $N = 1600$, and four different temperatures above but near the glass transition: (a) $T = 0.065p$, (b) $T = 0.06p$, (c) $T = 0.058p$, and (d) $T = 0.055p$. Each curve represents a different value of the overlap distance a. The range of overlap distances is the same as in the color plots of Fig. 4.1. The maximum of χ_{ss} with respect to a at each value of t is represented by the heavy, red curve. Circles mark the lag time $t^\star$ and amplitude $\chi^\star$ of local maxima of $\chi_{\mathrm{ss}}(a, t)$. As in Fig. 4.1, filled circles represent cage-breaking local maxima near the end of the sub-diffusive plateau of $\Delta r(t)$, and open circles represent cage-forming local maxima near the beginning of the plateau.
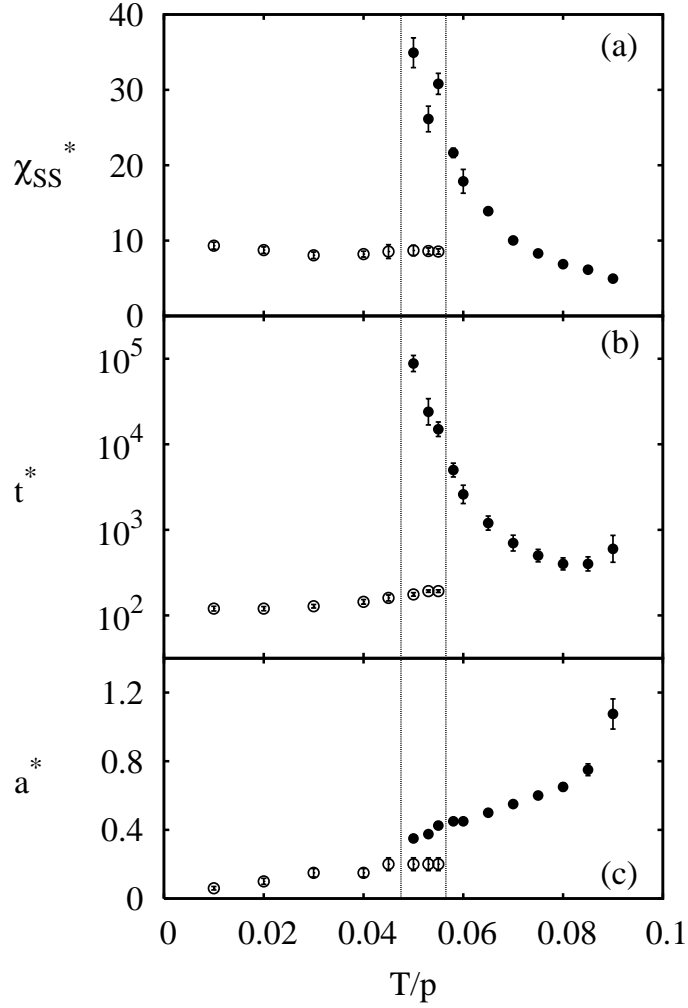
Figure 4.3: Local maxima of the dynamic susceptibility. We plot (a) the magnitudes of all observed local maxima of $\chi_{\mathrm{ss}}(a,t)$, $\chi^\star$, (b) their lag times $t^\star$, and (c) their overlap distances $a^\star$ as a function of temperature at fixed pressure $p = 10^{-2}$ and system size $N = 1600$. As in Fig. 4.1, the filled circles represent cage-escaping maxima, while the open circles represent cage-exploring maxima. The vertical dashed lines denote the range over which we observe both types of maxima. Note that (a) and (c) are presented on a linear scale, while (b) is presented on a log-linear scale. Error bars represent the larger of (1) the standard deviation of the mean calculated from simulations with different initial conditions and (2) the uncertainty associated with the discrete sampling of a and t.

time and space, $t^\star$, and $a^\star$, as functions of T at fixed pressure $p = 10^{-2}$ and system size $N = 1600$. The amplitude $\chi^\star$ and lag time $t^\star$ of the primary, cage-escaping maximum (solid symbols) both increase as T decreases until $t^\star$ passes beyond our observable time window.

The overlap distance $a^\star$ of the cage-escaping maximum is on the order of half a disk diameter for temperatures near the glass transition, a distance about two times larger than the plateau of the rms displacement. This distance presumably reflects the scale of the rearrangements necessary for diffusive motion to occur. At high temperatures above $T = 0.06p$, the plateau in the rms displacement is less well defined and the cage-escaping maximum lies at larger values of $a^\star$.

The temperature dependence of the cage-exploring, secondary maximum is markedly different from that of the primary maximum. Figure 4.3 shows that $\chi^\star$ and $t^\star$ remain roughly constant as temperature decreases from $T = 0.055p$, just above $T_g \approx 0.05p$, to $T = 0.01p$, which is well below it. This is consistent with the behavior of the rms displacement; the time of the onset of the plateau does not vary much with temperature as long as the temperature is low enough for the plateau to exist. The cage-exploring overlap distance $a^\star$ decreases with decreasing T, remaining near the plateau value in the rms displacement.

The amplitude $\chi^\star$ of the cage-escaping maximum is a measure of the number of disks whose dynamics are correlated at the crossover to diffusion, while $t^\star$ is a measure of the timescale for this longest, or α-, relaxation process. In Fig. 4.4 we plot $\chi^\star$, the number of disks whose dynamics are correlated at the cage-escaping maximum of χ_{ss}, as a function of the time scale corresponding to the cage-escaping maximum, $t^\star$. This time scale is a measure of the α-relaxation process. We have
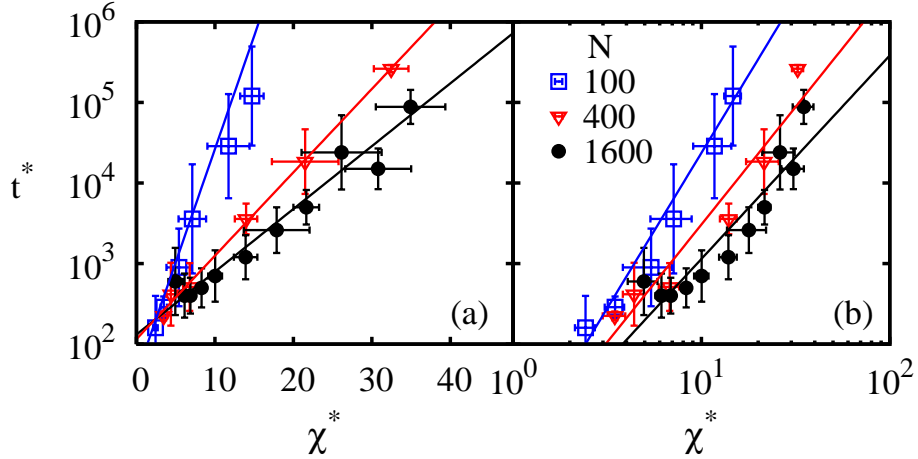
Figure 4.4: Dependence of the relaxation time $t^\star$ on the spatial extent of kinetic heterogeneities, $\chi^\star$. We plot the position of the cage-escaping maximum, $t^\star$ vs the magnitude of that maximum, $\chi^\star$ at fixed pressure $p = 10^{-2}$. Each point corresponds to a different temperature above T_g. Results are shown for three different system sizes N, as labelled, on both (a) a log-linear scale and (b) a log-log scale. The straight lines in (a) and (b) are exponential and power law fits, respectively. Error bars represent the larger of (1) the standard deviation of the mean calculated from simulations with different initial conditions and (2) the uncertainty associated with the discrete sampling of a and t.

plotted $\chi^\star$ vs. $t^\star$ for three different system sizes, $N = 100$, 400, and 1600. First, notice the substantial system-size dependence in $\chi^\star$ [58], even for temperatures for which the size of correlated regions $n^\star \approx 4\chi^\star$ is only on the order of 10. This indicates that the finite size of the system affects the dynamics even when the relative linear size of the correlated regions is as small as $\sqrt{n^\star/N} \approx 0.1$. This strong effect is likely due to a broad distribution of sizes of correlated regions. We find that while the spatial correlation function of the overlap function has an average correlation length consistent with the value $\sqrt{\pi \langle \sigma^2 \rangle n^\star/\phi}$ expected from a compact correlated region, it also has a long-ranged tail, decaying slower than

exponentially with distance. This long range tail reflects intermittent periods when the the clusters are extended. We find that $t^\star$ and $a^\star$ also depend on system size. If a is held fixed, $t^\star$ decreases and $\chi^\star$ increases with increasing system size N at all temperatures studied, consistent with Ref. [58]. However, when we maximize over a, we find that at sufficiently high T, $t^\star$ increases with N because $a^\star$ increases with N there.

For each system size N, however, the dependence of $\chi^\star$ on $t^\star$ is qualitatively similar. Note that the log-linear plot (Fig. 4.4(a)) is straighter than the log-log plot (Fig. 4.4(b)) for each system size, indicating that the dependence of $t^\star$ on $\chi^\star$ is described better by an exponential than by a power law. Such an exponential dependence of relaxation time on cluster size is expected in scenarios involving co-operative rearrangements [102]. Previous numerical studies of model glass formers fit $\chi^\star$ and $t^\star$ to power laws in $T - T_c$, where T_c is a critical temperature [41, 67, 99], implying that the relationship between $\chi^\star$ and $t^\star$ is also a power law. However, these studies determined $\chi^\star$ as the maximum of $\chi_4(a,t)$ with respect to t at fixed a, instead of searching for a maximum with respect to both t and a. Also, the relationship between $\chi^\star$ and $t^\star$ was not shown directly. An analysis of a lower bound of χ_4 for several real glass-forming liquids found an exponential dependence near the glass transition [26], consistent with our results.

In this chapter, we quantified the size of kinetic heterogeneities for a model glass-forming liquid as a function of temperature by measuring fluctuations of a dynamic order parameter. By measuring the dynamic susceptibility $\chi_{ss}(a,t)$ as a function of both lag time and overlap distance, we identified two distinct local maxima. The primary, "cage-escaping" maximum, which has been found in pre-

vious numerical and experimental studies, occurs at the end of the plateau in the root-mean-square displacement, near the onset of diffusive transport. We also discovered a secondary, "cage-exploring" maximum at the beginning of the plateau in the mean-squared displacement, which corresponds to the ballistic to sub-diffusive crossover. Thus, the dynamics are most heterogeneous at displacements and times corresponding to crossovers in the dynamics.

The secondary, cage-exploring maximum at the crossover from ballistic to sub-diffusive motion emerges from the shoulder of the primary cage-escaping maximum when the temperature is low enough that there is a well-defined plateau in the mean-squared displacement. We find that the plateau must extend over at least two orders of magnitude in order for the cage-exploring maximum to appear. We observe both maxima over the range of temperatures low enough that the mean-squared displacement exhibits a broad plateau but high enough that the eventual crossover to the diffusive regime is still observable. Note that although both maxima emerge, grow, and shift continuously with temperature, there is an apparent discontinuous drop in the largest observed maximum at the dynamical glass transition. This occurs when the primary maximum passes out of observation range, leaving only the secondary, cage-exploring maximum (see Fig. 4.3(b)).

While the crossover from sub-diffusive to diffusive motion measures the approach to the glass transition, the crossover from ballistic to sub-diffusive motion is a general and relatively innocuous feature of dense fluids and solids. Our finding that both crossovers exhibit maxima in the dynamic susceptibility suggests that spatially heterogeneous dynamics are a general feature of dynamical crossovers caused by interactions. Indeed, a crystalline system of monodisperse disks ex-

79

hibits a cage-exploring maximum at the end of the ballistic regime that is similar to the one shown here. We suspect that more exotic dynamical crossovers, like those between two diffusive regimes with different diffusion coefficients, should also exhibit kinetic heterogeneities. The existence of kinetic heterogeneities is therefore a general feature of dynamical crossovers and should not necessarily be taken as a sign of an impending glass transition.

Chapter 5

Conclusion

By measuring relaxation times, rheology, and fluctuations for a class of model glass-forming fluids, we have identified common mechanisms responsible for fluidization of finite-range, repulsive particles under the combined effects of pressure p, temperature T, and applied shear stress σ. We have demonstrated that repulsive particles may be organized in a jamming phase diagram parameterized by the dimensionless quantities T/pd^3, σ/p, and pd^3/ϵ, where d is the linear size of the particles and ϵ is the interaction energy scale. The jamming phase diagram describes the three-dimensional parameter space as the product of an equilibrium plane at $\sigma/p = 0$ and a hard sphere plane at $pd^3/\epsilon = 0$. Near the hard sphere plane, the jamming phase diagram is universal in the sense that material properties are insensitive to the details of the interaction potential. Using a dimensionless relaxation time as the order parameter for the jamming phase diagram, we constructed a two-dimensional dynamic glass transition surface whose precise location depends on an arbitrary time scale but always encloses the singular point

at the origin, $T/pd^3 = \sigma/p = pd^3/\epsilon = 0$.

In order for the jamming phase diagram picture to be useful, it should reveal common mechanisms for slow dynamics as the dynamic glass transition surface is approached along various paths. The establishment of the dimensionless jamming phase diagram already demonstrates that over a range of parameter space, the approach to the dynamic glass transition is controlled by the same mechanism, a competition between thermal fluctuations and the pressure, along paths of increasing temperature and decreasing pressure. In order to extend this framework away from the equilibrium plane, we investigated how the effective temperature controls material properties of soft and hard spheres under a combination of temperature and applied stress. We demonstrated that the dynamic glass transition surface is largely controlled by the competition between low frequency fluctuations and the confining pressure. Even well into the fluid portion of the jamming phase diagram, we find that relaxation is largely controlled by a single measure of these low frequency fluctuations, the effective temperature, regardless of whether the fluctuations are created by temperature or shear.

Finally, by investigating correlations in the dynamics, we make some progress in understanding why the dynamics slow down so dramatically as the strength of fluctuations decreases. By measuring a dynamic susceptibility as a function of both time and length scale, we obtain among other results an improved measurement of the relation between relaxation time and the spatial extent of correlated dynamics, indicating that the relaxation time depends exponentially on the number of particles that must move in a correlated manner.

Appendix A

Simulation Methods

A.1   Hard Sphere Algorithm

To solve the dynamics of hard spheres, we use an event-driven algorithm following Marin, Risso, and Cordero [74]. The algorithm determines each subsequent collision by maintaining a future events list organized in a binary tree. At the base (0th level) of the tree are N local minimum events corresponding to the N hard spheres in the system. Each local minimum event consists of a time and a partner for a future collision. These local minimum events in turn are the top entry of N local lists, one for each sphere, which are ordered by time so that the top entry is the one with the earliest future time. The future events list is organized like a sports tournament into a binary tree where the ith level consists of $N/2^i$ entries, each entry determined by whichever of its two downstream entries has an earlier time. After each collision, necessary updates are performed, then the next event is determined as the event at the top of the binary tree.

New future collisions are determined only as often as necessary to maintain the accuracy of the top of the binary tree, not so often as to maintain the accuracy of the entire binary tree and the local lists. The frequency of future collision calculations is reduced by using the extended exclusive particle grid method developed by Isobe [55]. The simulation cube is divided into a grid of cells, each cell sufficiently small that it can only contain at most one sphere center. At any given time, each sphere is uniquely associated with one of the cells. Updating an association means associating a sphere with the cell containing its center. The grid facilitates the calculation of future collisions by directing the search to a small number of neighboring cells called the mask. The size of the mask must be optimized for speed. For instance, we found that for bidisperse disks in two dimensions or monodisperse spheres in three dimensions, a mask of width 7 cells is optimal, while for bidisperse spheres in three dimensions, a mask of width 9 cells is optimal. Too small a mask reduces speed because the cell associations must be re-calculated whenever a sphere moves a distance on the order of the mask width; too large a mask reduces speed because too many future collisions are calculated.

A.2   Soft Sphere Algorithm

To determine the dynamics of soft spheres of dimensionality d at fixed temperature T, pressure p, and shear strain rate $\dot{\gamma}$, we conduct molecular dynamics simulations solving the Sllod equations of motion with Lees-Edwards periodic boundary conditions. We employ Gaussian constraints [33, 34, 53] to fix the instantaneous temperature $T = |\vec{p_i}|^2/d(N-1)$ and hydrostatic pressure $p = (\vec{r_i} \cdot \vec{F_i}/2 + NT)/L^d$,

where $\vec{F}_i = -\vec{\nabla} \sum_j V(r_{ij})$ and repeated indices are summed. In doing so we measure the particle momenta $\vec{p}_i$ relative to an imposed uniform shear gradient and allow the side length L of the periodic cell to vary. The equations of motion are:

$$
\begin{aligned}
\dot{\vec{r}}_i &= \vec{p}_i + \dot{\gamma} r_{yi} \hat{e}_x + \dot{\kappa} \vec{r}_i, \\
\dot{\vec{p}}_i &= \sum_j \vec{F}_i - \dot{\gamma} p_{yi} \hat{e}_x - \dot{\kappa} \vec{p}_i - \alpha \vec{p}_i, \\
\dot{L} &= \dot{\kappa} L.
\end{aligned}
\tag{A.1}
$$

The Gaussian constraints satisfy the equations

$$
\begin{aligned}
\alpha &= \frac{\vec{p}_i \cdot \vec{F}_i - \dot{\gamma} p_{ix} p_{iy}}{|\vec{p}_i|^2} - \dot{\kappa} - \frac{\dot{T}}{2T}, \\
\dot{\kappa} &= \frac{-\sum_{i<j} \Phi_{ij}(\vec{r}_{ij} \cdot \vec{p}_{ij} + \dot{\gamma} r_{xij} r_{yij}) - dL^d \dot{p} + dN\dot{T}}{d^2 p L^d + \sum_{i<j} \Phi_{ij} |\vec{r}_{ij}|^2},
\end{aligned}
\tag{A.2}
$$

where $\Phi_{ij} = V'(r_{ij})/r_{ij} + V''(r_{ij})$ and $\vec{p}_{ij} = \vec{p}_i - \vec{p}_j$. The temperature and pressure are invariants of these equations of motion when $\dot{T} = \dot{p} = 0$, but because of the stiffness of the equations of motion, the pressure would drift due to accumulated numerical error unless corrected. We employ a proportional feedback mechanism to cancel this effect [8], setting $\dot{T} = \omega_T(T_0 - T)$ and $\dot{p} = \omega_p(p_0 - p)$. We use $\omega_T = 0.1$ and $\omega_p = 10$, which are large enough to keep the variance in the pressure about 10^5 times smaller than its constant-volume value but small enough to allow us to use a reasonably large time step of size 0.005.

Bibliography

[1] A. R. Abate and D. J. Durian. Phys. Rev. E **76**, 021306, 2007.

[2] C. Alba-Simionesco, D. Kivelson, and G. Tarjus. J. Chem. Phys. **116**, 5033, 2002.

[3] B. J. Alder, D. M. Gass, and T. E. Wainwright. J. Chem. Phys. **53**, 3813, 1970.

[4] M. P. Allen and D. J. Tildesley. Computer Simulation of Liquids. Oxford University Press, New York, 1987.

[5] H. C. Andersen. Proc. Natl. Acad. Sci. U.S.A. **102**, 6686, 2005.

[6] C. A. Angell. Science **267**, 1924, 1995.

[7] N. W. Ashcroft and D. C. Langreth. Phys. Rev. **156**, 685, 1967.

[8] A. Baranyai and D. J. Evans. Mol. Phys. **70**, 53, 1990.

[9] J. A. Barker and D. Henderson. J. Chem. Phys. **47**, 4714, 1967.

[10] J.-L. Barrat and L. Berthier. Phys. Rev. E **63**, 012503, 2000.

[11] L. Berthier and J.-L. Barrat. J. Chem. Phys. **116**, 6228, 2002.

[12] L. Berthier and J.-L. Barrat. Phys. Review Letters **89**, 095702, 2002.

[13] L. Berthier, J.-L. Barrat, and J. Kurchan. Phys. Rev. E **61**, 5464, 2000.

[14] L. Berthier, G. Biroli, J.-P. Bouchaud, L. Cipelletti, D. El Masri, D. L'Hôte, F. Ladieu, and M. Pierno. Science **310**, 1797, 2005.

[15] L. Berthier, G. Biroli, J.-P. Bouchaud, W. Kob, K. Miyazaki, and D. R. Reichman. J. Chem. Phys. **126**, 184503, 2007.

[16] L. Berthier, G. Biroli, J.-P. Bouchaud, W. Kob, K. Miyazaki, and D. R. Reichman. J. Chem. Phys. **126**, 184504, 2007.

[17] L. Berthier and T. A. Witten. EPL **86**, 10001, 2009.

[18] R. Böhmer, K. L Ngai, C. A. Angell, and D. J. Plazek. J. Chem. Phys. **99**, 4201, 1993.

[19] D. Chandler, J. P. Garrahan, R. L. Jack, L. Maibaum, and A. C. Pan. Phys. Rev. E **74**, 051501, 2006.

[20] D. Charbonneau and D. R. Reichman. Phys. Rev. Lett. **99**, 135701, 2007.

[21] L. Cipelletti and L. Ramos. J. Phys. Condens. Matter **17**, R253, 2005.

[22] M. Cloitre, R. Borrega, F. Monti, and L. Leibler. Phys. Rev. Lett. **90**, 068303, 2003.

[23] E. I. Corwin, H. M. Jaeger, and S. R. Nagel. Nature (London) **435**, 1075, 2005.

[24] L. F. Cugliandolo, J. Kurchan, and L. Peliti. Phys. Rev. E **55**, 3898, 1997.

[25] F. da Cruz, S. Emam, M. Prochnow, J.-N. Roux, and F. Chevoir. Phys. Rev. E **72**, 021309, 2005.

[26] C. Dalle-Ferrier, C. Thibierge, C. Alba-Simionesco, L. Berthier, G. Biroli, J.-P. Bouchaud, F. Ladieu, D. L'Hôte, and G. Tarjus. Phys. Rev. E **76**, 041510, 2007.

[27] T. Danino and A. J. Liu. Unpublished.

[28] J. Delhommelle, J. Petravic, and D. J. Evans. Phys. Rev. E **68**, 031201, 2003.

[29] D. J. Durian. Phys. Rev. Lett. **75**, 4780, 1995.

[30] D. J. Durian. Phys. Rev. E **55**, 1739, 1997.

[31] M. D. Ediger, C. A. Angell, and S. R. Nagel. J. Chem. Phys. **100**, 1996.

[32] Y. S. Elmatad, D. Chandler, and J. P. Garrahan. J. Phys. Chem. B **113**, 5563, 2009.

[33] D. J. Evans and G. P. Morriss. Chem. Phys. **77**, 63, 1983.

[34] D. J. Evans and G. P. Morriss. Phys. Lett. **98A**, 433, 1983.

[35] D. J. Evans and G. P. Morriss. Phys. Rev. Lett. **56**, 2172, 1986.

[36] M. L. Falk and J. S. Langer. Phys. Rev. E **57**, 7192, 1998.

[37] E. Flenner and G. Szamel. J. Phys. Condens. Matter **19**, 205125, 2007.

[38] Y. Forterre and O. Pouliquen. Annu. Rev. Fluid Mech. **40**, 1, 2008.

[39] R. Garcia-Rojo. Phys. Rev. E **74**, 2006.

[40] S. C. Glotzer. J. Non-Crystalline Solids **274**, 342, 2000.

[41] S. C. Glotzer, V. N. Novikov, and T. B. Schrøder. J. Chem. Phys. **112**, 509, 2000.

[42] A. D. Gopal and D. J. Durian. J. Colloid Interface Sci. **213**, 169, 1999.

[43] P. Guan, M. Chen, and T. Egami. Phys. Rev. Lett. **104**, 205701, 2010.

[44] J. P. Hanson and I. R. McDonald. Theory of Simple Liquids. Academic, London, 1976.

[45] T. Hatano. J. Phys. Soc. Jpn. **77**, 123002, 2008.

[46] T. K. Haxton and A. J. Liu. In preparation.

[47] T. K. Haxton and A. J. Liu. Submitted to EPL (arXiv:1002.0520v1).

[48] T. K. Haxton and A. J. Liu. Phys. Rev. Lett. **99**, 195701, 2007.

[49] T. K. Haxton, M. Schmiedeberg, and A. J. Liu. In preparation.

[50] E. Helfand. Phys. Rev. **119**, 1, 1960.

[51] Y. Hiwatari and T. Muranaka. J. Non-Crystalline Solids **235**, 19, 1998.

[52] R. Höhler and S. Cohen-Addad. J. Phys. Condens. Matter **17**, R1041, 2005.

[53] L. M. Hood, D. J. Evans, and H. J. M. Hanley. J. Stat. Phys. **57**, 729, 1989.

[54] P. Ilg and J.-L. Barrat. Europhys. Lett. **79**, 26001, 2007.

[55] M. Isobe. Int. J. Mod. Phys. C **10**, 1281, 1999.

[56] H. Jónsson and H. C. Andersen. Phys. Rev. Lett. **60**, 2295, 1988.

[57] R. D. Kamien and A. J. Liu. Phys. Rev. Lett. **99**, 155501, 2007.

[58] S. Karmakar, C. Dasgupta, and S. Sastry. Proc. Natl. Acad. Sci. U.S.A. **106**, 3675, 2009.

[59] K. Kawasaki and J. D. Gunton. Phys. Rev. A **8**, 2048, 1973.

[60] J. G. Kirkwood and F. P. Buff. J. Chem. Phys. **19**, 774, 1951.

[61] W. Kob and H. C. Andersen. Phys. Rev. E **51**, 4626, 1995.

[62] W. Kob, F. Sciortino, and P. Tartaglia. Europhys. Lett. **49**, 590, 2000.

[63] J. S. Langer. Phys. Rev. E **70**, 041502, 2004.

[64] J. S. Langer and M. L. Manning. Phys. Rev. E **76**, 056107, 2007.

[65] J. S. Langer and L. Pechenik. Phys. Rev. E **68**, 061507, 2003.

[66] S. A. Langer and A. J. Liu. Europhys. Lett. **49**, 68, 2000.

[67] N. Lačević, F. W. Starr, T. B. Schrøder, and S. C. Glotzer. J. Chem. Phys. **119**, 7372, 2003.

[68] F. Lechenault, O. Dauchot, G. Biroli, and J. P. Bouchaud. Europhys. Lett. **83**, 46003, 2008.

[69] A. Lemaître. Phys. Rev. Lett. **89**, 195503, 2002.

[70] A. J. Liu and S. R. Nagel. Nature (London) **396**, 21, 1998.

[71] J. Lu, G. Ravichandran, and W. L. Johnson. Acta Mater. **51**, 3429, 2003.

[72] H. A. Makse and J. Kurchan. Nature (London) **415**, 614, 2002.

[73] C. Maloney and A. Lemaître. Phys. Rev. Lett. **93**, 016001, 2004.

[74] M. Marin, D. Risso, and P. Cordero. J. Comp. Phys. **109**, 306, 1993.

[75] T. G. Mason, J. Bibette, and D. A. Weitz. J. Colloid Interface Sci. **179**, 439, 1996.

[76] J. Matsui, M. Fujisaki, and T. Odagaki. J. Non-Crystalline Solids **235**, 335, 1998.

[77] J. Matsui, T. Odagaki, and Y. Hiwatari. Phys. Rev. Lett. **73**, 2452, 1995.

[78] C. S. O'Hern, A. J. Liu, and S. R. Nagel. Phys. Rev. Lett. **93**, 165702, 2004.

[79] C. S. O'Hern, L. E. Silbert, A. J. Liu, and S. R. Nagel. Phys. Rev. E **68**, 011306, 2003.

[80] P. Olsson and S. Teitel. Phys. Rev. Lett. **99**, 178001, 2007.

[81] I. K. Ono, C. S. O'Hern, D. J. Durian, S. A. Langer, A. J. Liu, and S. R. Nagel. Phys. Rev. Lett. **89**, 095703, 2002.

[82] L. S. Ornstein and F. Zernike. Physik. Z. **19**, 134, 1918.

[83] M. Otsuki and H. Hayakawa. Phys. Rev. E **80**, 011308, 2009.

[84] G. Parisi and F. Zamponi. Rev. Mod. Phys. **82**, 789, 2010.

[85] G. Petekidis, D. Vlassopoulos, and P. N. Pusey. J. Phys. Condens. Matter **16**, S3955, 2004.

[86] P. Peyneau and J. Roux. Phys. Rev. E **78**, 011307, 2008.

[87] F. Q. Potiguar and H. A. Makse. Eur. Phys. J. E **19**, 171, 2006.

[88] R. Richert. J. Phys. Condens. Matter **14**, R703, 2002.

[89] C. M. Roland, S. Hensel-Bielowska, M. Paluch, and R. Casalini. Rep. Prog. Phys. **68**, 1405, 2005.

[90] M. Schmiedeberg, T. K. Haxton, S. R. Nagel, and A. J. Liu. In preparation.

[91] J. R. Seth, M. Cloitre, and R. T. Bonnecaze. J. Rheol. **50**, 353, 2006.

[92] Y. Shokef and D. Levine. Phys. Rev. E **74**, 051111, 2006.

[93] L. E. Silbert, A. J. Liu, and S. R. Nagel. Phys. Rev. Lett. **95**, 098301, 2005.

[94] L. E. Silbert, A. J. Liu, and S. R. Nagel. Phys. Rev. E **73**, 041304, 2006.

[95] A. P. Sokolov, U. Buchenau, W. Steffen, B. Frick, and A. Wischnewski. Phys. Rev. B **52**, R9815, 1995.

[96] P. Sollich, F. Lequeux, P. Hébraud, and M. E. Cates. Phys. Rev. Lett. **78**, 2020, 1997.

[97] C. Song, P. Wang, and H. A. Makse. Proc. Natl. Acad. Sci. U.S.A. **102**, 2299, 2005.

[98] F. H. Stillinger and T. A. Weber. Phys. Rev. A **25**, 978, 1982.

[99] G. Szamel and E. Flenner. Phys. Rev. E **74**, 021507, 2006.

[100] G. Tarjus, D. Kivelson, S. Mossa, and C. Alba-Simionesco. J. Chem. Phys. **120**, 6135, 2004.

[101] S. Tewari, D. Schiemann, D. J. Durian, C. M. Knobler, S. A. Langer, and A. J. Liu. Phys. Rev. E **60**, 4385, 1999.

[102] C. Toninelli, M. Wyart, L. Berthier, G. Biroli, and J.-P. Bouchaud. Phys. Rev. E **71**, 041505, 2005.

[103] P. Wang, C. Song, C. Briscoe, and H. A. Makse. Phys. Rev. E **77**, 061309, 2008.

[104] S. Webb. Rev. Geophys. **35**, 191, 1997.

[105] S. L. Webb and D. B. Dingwell. J. Geophys. Res. **95**, 15695, 1990.

[106] J. D. Weeks, D. Chandler, and H. C. Andersen. J. Chem. Phys. **54**, 5237, 1971.

[107] K. Z. Win and N. Menon. Phys. Rev. E **73**, 040501, 2006.

[108] M. Wyart, S. R. Nagel, and T. a. Witten. Europhys. Lett. **72**, 486, 2005.

[109] M. Wyart, L. E. Silbert, S. R. Nagel, and T. A. Witten. Phys. Rev. E **72**, 051306, 2005.

[110] N. Xu, T. K. Haxton, A. J. Liu, and S. R. Nagel. Phys. Rev. Lett. **103**, 245701, 2009.

[111] P. Xu, T. Cagin, and W. A. Goddard III. J. Chem. Phys. **123**, 104506, 2005.

[112] R. Zondervan, T. Xia, H. van der Meer, C. Storm, F. Kulzer, W. van Saarloos, and M. Orrit. Proc. Natl. Acad. Sci. U.S.A. **105**, 2008.